UNIVERSITY OF CALIFORNIA,
IRVINE

Modeling, Design Exploration, and Optimization of Shape Memory Alloy Axial Actuators

THESIS

submitted in partial satisfaction of the requirements
for the degree of

MASTER OF SCIENCE

in Mechanical and Aerospace Engineering

by

Weilin Guan

Thesis Committee:
Professor Mark E. Walter, Chair
Assistant Professor Ramin Bostanabad
Assistant Professor Penghui Cao

2021

TABLE OF CONTENTS

LIST OF FIGURES

LIST OF TABLES

ACKNOWLEDGMENTS

First and foremost, I am sincerely grateful to my advisor Dr. Edwin Peraza Hernandez for his continuous guidance and support on my research study. I would like thank Dr. Hernandez for providing me with the opportunity to join his research group and perform high-impact research. I learned a lot from Dr. Hernandez through the countless hours of insightful discussions we had and his reviewing of my research manuscripts meticulously. His endless encouragement and inspiring advice empowered me to strengthen my critical engineering and technical communication skills. My exposure to multifunctional materials and adaptive structures through working with Dr. Hernandez profoundly shaped my research objectives and career path. I feel extremely honored to have Dr. Hernandez as my advisor and mentor.

I would also like to thank Dr. Mark E. Walter, my committee chair, for introducing me to continuum mechanics and the inspiring guidance on principles of engineering that vastly improved my approach to tackle various research problems. I would like to extend my gratitude to Dr. Penghui Cao and Dr. Ramin Bostanabad for agreeing to be my committee members. The friendly attitude and patience in explaining new concepts of Dr. Cao allowed me to learn a lot through his atomistics theory and material failure and fracture classes. Although I have not had the chance to attend a class instructed by Dr. Bostanabad, his constructive comments enabled me improve my engineering problem solving skills.

My appreciation extends to my fellow colleagues in the Morphing Structures Group at UC Irvine. I especially thank Hasitha Hewakuruppu and Nguyen (Tony) Pham for our wonderful research collaborations. Their assistance allowed me to improve my teamwork skills and be a better researcher. I would like to acknowledge the undergraduate students in the Tensegrity Wing team for their contribution on the fabrication of the tensegrity wing prototype that was leveraged in my research work.

I want to thank my parents Meilian Cai and Yaobo Guan for their unconditional love and encouragement through the successes and challenges I encounter during all these years. My accomplishments thus far would not have been possible without their continuous support.

Lastly, I would like to thank the American Society of Mechanical Engineers and the Society of Photo-optical Instrumentation Engineers for giving me permission to incorporate my previously published works into this thesis.

VITA

Weilin Guan

EDUCATION

Master of Science in Mechanical and Aerospace Engineering **Fall 2021**
University of California, Irvine *Irvine, California*

Bachelor of Science in Mechanical Engineering **June 2020**
University of California, Irvine *Irvine, California*

RESEARCH EXPERIENCE

Graduate Researcher **2020–2021**
Morphing Structures Group, University of California, Irvine *Irvine, California*

Undergraduate Researcher **2019–2020**
Morphing Structures Group, University of California, Irvine *Irvine, California*

PROFESSIONAL EXPERIENCE

"Hybrid Renewable Energy System" Project **2020**
Earth, Elements & Energy Inc. *Culver City, California*

"Waste to Energy" Project **2019**
Meggitt *Akron, Ohio*

SERVICE AND OUTREACH

Teaching Assistant, Mechanics of Structures	Fall 2021
Course Assistant, Mechanics of Smart Structures	Spring 2021
Solid Mechanics Graduate Student Seminar Organizer and Host	2020 - 2021
Manuscript Reviewer, IDETC-CIE	2020 - 2021
Speaker, SMASIS High School Outreach Activity	2020 - 2021
Volunteer, Project Grow (Ecological Restoration Program)	2018

PUBLICATIONS

Machine learning-assisted modeling and design optimization of hybrid shape memory alloy axial actuators **Sep 2021**

Proceedings of the ASME 2021 Conference on Smart Materials, Adaptive Structures and Intelligent Systems, SMASIS2021-68340, virtual conference. https://doi.org/10.1115/SMASIS2021-68340

Weilin Guan, Hasitha J. Hewakuruppu, and Edwin A. Peraza Hernandez

Planning laser-forming folding motion with thermal simulation **May 2021**

Proceedings of the 2021 IEEE International Conference on Robotics and Automation (ICRA), pp. 7788-7794. https://doi.org/10.1109/ICRA48506.2021.9561883

Yue Hao, Weilin Guan, Edwin A. Peraza Hernandez, and Jyh-Ming Lien

Design exploration of a tensegrity twisting wing enabled by shape memory alloy wire actuation **Mar 2021**

Proceedings of SPIE Smart Structures/NDE 2021, Active and Passive Smart Structures and Integrated Systems XV, 1158809, virtual conference. https://doi.org/10.1117/12.2582829

Weilin Guan, Nguyen K. Pham, and Edwin A. Peraza Hernandez

Design framework for multi-section shape memory alloy axial actuators considering material and geometric uncertainties **Aug 2020**

Proceedings of the ASME 2020 International Design Engineering Technical Conference & Computers and Information in Engineering Conference (IDETC/CIE 2020), DETC2020-22683, virtual conference. https://doi.org/10.1115/DETC2020-22683

Weilin Guan and Edwin A. Peraza Hernandez

HONORS AND AWARDS

Honorable Mention, National Science Foundation Graduate Research Fellowships Program (NSF GRFP)	2021
Second place, Best Student Paper Award Competition at the SPIE Smart Structures/NDE 2021 Conference	2021
Graduate Assistance in Areas of National Need Fellowship	2020
UC Irvine Minority Serving Institution Enhancement Award	2020
UC Irvine Diversity Recruitment Fellowship	2020
Magna Cum Laude (B.S. in Mechanical Engineering)	2020
Undergraduate Research Opportunities Program Grant	2020
Tau Beta Pi (Engineering Honors Society)	2018
Dean's Honors List (10 quarters during undergraduate studies)	2016-2020

ABSTRACT OF THE THESIS

Modeling, Design Exploration, and Optimization of Shape Memory Alloy Axial Actuators

By

Weilin Guan

Master of Science in Mechanical and Aerospace Engineering

University of California, Irvine, 2021

Professor Mark E. Walter, Chair

This thesis presents a modeling, design exploration, and optimization study of novel shape memory alloy (SMA) axial actuators. Shape memory alloys are materials that can generate and recover moderate inelastic strains through temperature modulation and exhibit high actuation energy density compared to other smart material actuators. This characteristic enables SMAs to function as lightweight and compact thermomechanical actuators. The synthesis of SMA actuators for systems with specific requirements on their actuation path (displacement stroke vs. temperature) currently relies on complex and expensive material processing and characterization. First, a geometric approach for synthesizing novel SMA axial actuators, termed as hybrid SMA actuators, whose dimensions and material distribution are modulated to approximate a target actuation path. Through the combination of multiple SMA wire sections in series, the hybrid SMA actuators can exhibit actuation paths not achievable by using single monolithic SMA wires. A reduced-order numerical model for the hybrid SMA actuators that allows for efficient design evaluations is derived and implemented. An approach to incorporate uncertainty in the parameters of the actuators within the design framework is implemented to allow for the determination of robust actuator designs. A machine learning-assisted framework for the surrogate modeling of hybrid SMA actuators is then detailed. This approach allows for the prediction of their actuation path without the use of structural simulations leveraging numerical implementations of constitutive models,

allowing for simplified and computationally efficient modeling and circumventing convergence issues. A surrogate model consisting of an ensemble of binary decision trees is trained using data obtained via a design of experiments performed using structural simulations. A validation test using 5000 design samples for hybrid SMA actuators with two sections demonstrates R^2 values of 0.99983 and 0.99979 for the actuation displacement during heating and cooling, respectively. The evaluation time for the validation samples using the trained surrogate model is less than 8 minutes, while the evaluation time using structural simulations is 59 minutes. A surrogate-based optimization approach is then demonstrated through the synthesis of hybrid SMA actuators capable of exhibiting prescribed target actuation paths. Lastly, a modeling, experimental prototyping, and computational design exploration study of a morphing wing enabled by a tensegrity mechanism and actuated by shape memory alloy (SMA) wires is investigated. The studied wing design circumvents conventional control surfaces such as hinged flaps and ailerons through the implementation of a smooth wing shape that twists to modulate its flight characteristics. The continuous and smooth wing surface lessens aerodynamic drag to enhance aerodynamic efficiency. The morphing capability of the wing is enabled through an integrated lightweight tensegrity mechanism, which provides twisting motion through elongation/contraction of the SMA wires. Befitting for the actuation of the tensegrity mechanism due to their rod form, SMA wire actuators are incorporated to reconfigure the wing shape through thermally driven material actuation. A finite element model that integrates the wing, tensegrity mechanism, and SMA wire actuators is created to assess the stresses, maximum attainable twist angle, and structural mass of the wing. A design of experiment study is performed to evaluate the influence of the topological and geometrical design parameters on performance responses such as twist angle and mass. The most favorable design demonstrates a maximum twist angle of 15.85° and a mass of 2.02 kg without exceeding the material stress limits. The SMA-enabled torsional morphing capability is also demonstrated experimentally through a tensegrity twisting wing prototype equipped with commercially available SMA wire actuators.

Chapter 1

Introduction

[1] [2] [3] This chapter provides an introduction to and literature review of the topics and concepts presented in the subsequent chapters of this thesis. An introduction to shape memory alloys and their application as actuators is presented in Section 1.1. Section 1.2 details a geometric approach to the modulation of the actuator response. Section 1.3 proceeds to describe the implementation of machine learning techniques towards the modeling process. A morphing wing enabled by SMA actuation is explored in Section 1.4. Lastly, Section 1.5 details the contributions of this thesis and lays out the structure of the remainder of the thesis.

[1]Portions of this chapter are reprinted or adapted from [Weilin Guan and Edwin A. Peraza Hernandez, 2020, "Design framework for multi-section shape memory alloy axial actuators considering material and geometric uncertainties," Proceedings of the ASME 2020 International Design Engineering Technical Conferences and Computers and Information in Engineering Conference, DETC2020-22683. https://doi.org/10.1115/DETC2020-22683]. Figures and texts are reprinted by permission of the American Society of Mechanical Engineers.

[2]Portions of this chapter are reprinted or adapted from [Weilin Guan, Hasitha J. Hewakuruppu, and Edwin A. Peraza Hernandez, 2021, "Machine learning-assisted modeling and design optimization of hybrid shape memory alloy axial actuators," Proceedings of the ASME 2021 Conference on Smart Materials, Adaptive Structures and Intelligent Systems, SMASIS2021-68340. https://doi.org/10.1115/SMASIS2021-68340]. Figures and texts are reprinted by permission of the American Society of Mechanical Engineers.

[3]Portions of this chapter are reprinted or adapted from [Weilin Guan, Nguyen K. Pham, and Edwin A. Peraza Hernandez, 2021, "Design exploration of a tensegrity twisting wing enabled by shape memory alloy wire actuation," Proceedings of SPIE Smart Structures/NDE 2021, Active and Passive Smart Structures and Integrated Systems XV, 1158809, virtual conference. https://doi.org/10.1117/12.2582829]. Figures are reprinted by permission of the American Institute of Aeronautics and Astronautics, Inc.

1.1 Shape Memory Alloys

Shape memory alloys (SMAs) are active materials with the ability to repeatedly generate and recover inelastic strains driven by changes in temperature and stress [7]. This behavior, along with their stiffness typical of metallic systems, allows SMAs to concurrently function as structural components and actuators [8, 21]. While being lightweight and compact, SMA wires can provide high energy per unit volume actuation as axial actuators and high displacement stroke as coil spring actuators [26, 29]. As potential candidates to replace the bulky hydraulic, pneumatic, and electric actuators, SMA wire actuators are superior as they provide silent and smooth operations [47]. Shape memory alloy wire actuators operate through reversible axial strain due to material transformation that is dictated by temperature variation, which can be applied via Joule heating. Thus, they function as thermal actuators of simple geometry that enables easy maintenance [45]. These characteristics support the increasing demand for design, modeling, and applications of SMA actuators in the aerospace, automotive, biomedical, and defense sectors [16, 38]. The integration of SMA actuators into existing systems that incorporate conventional actuator options to reduce their complexity and to enhance efficiency. In recent years, SMA actuators have also been exploited for applications including morphing wings [43] and microrobotics [56].

The operation of SMA actuators relies on solid-to-solid material transformation. The SMA materials transition between a compact austenite phase at high temperatures and a shear and stretched martensite phase at low temperatures which induce shape deformation. The forward transformation denotes the transition from austenite to martensite while the reverse transformation denotes the opposite direction. However, the forward and reverse transformations occurring at different temperatures lead to nonlinear and hysteretic SMA transformations [3, 9].

A current challenge in designing SMA actuators is to enable efficient and inexpensive mod-

ification of their transformation hysteresis to adapt to different applications. For instance, morphing wings enabled by SMA actuation require wide SMA transformation ranges while thermal regulators benefit from a narrow SMA transformation range to behave as an on-off switch [34]. This is often accomplished through material processing and manufacturing methods to produce customized SMA material designs. However, this material engineering approach is expensive and challenging to scale [1]. Shape memory alloys exhibit high sensitivity as minuscule variation in their material composition may dramatically alter their hysteresis and other material properties [20]. This uncertainty complicates the SMA actuator design process for applications that demand a precise hysteretic path. This approach is also inefficient as the material properties (*e.g.,* conductivity, plasticity, and fatigue) are unknown for a newly developed SMA material. Subsequently, comprehensive material testing is necessary for each customized SMA design, which further increases their cost and delays the practical application [17].

This work first introduces a design approach for synthesizing the novel *hybrid SMA actuators*, which consist of multiple distinctive wire sections connected in series. The wire sections are aligned concentrically and connected axially at the wire ends using metallic wire crimp connectors for the fabrication of the hybrid SMA actuators. The individual actuator sections can be modulated geometrically through their section length and cross-sectional area and assigned different SMA materials based on commercially available options. These design parameters are optimized so that the global actuation response approximates a target displacement vs. temperature path. Selden *et al.* bypassed the material engineering approach through the geometrical modulation of SMA actuators such that the SMA wire actuator was divided into multiple segments to control the temperature individually to obtain a desired global hysteretic behavior [49]. The approach presented in this work is based on uniform temperature among the actuator sections where the temperature adjustment occurs globally. The optimization process considers constraints, including the minimum length-to-diameter aspect ratio and the maximum stress of the actuator sections.

The computational approach to accomplish the actuator design task is to optimize the design parameter combination corresponding to different actuator responses modeled using constitutive SMA models. The process of modeling the actuator response consumes the majority of the computation time, which increases drastically as the number of design variables increases with the number of actuator sections. Implicit and explicit numerical methods represent the conventional analytical implementations. The implicit method outweighs the explicit method, which results in longer computation time for modeling the actuator response as very small temperature increments are necessary to cover the heating and cooling cycles due to the conditional stability requirement. Thus, an implicit approach was implemented initially as detailed in Section 2.2 for the modeling of the actuator response. The implicit approach provides solving the global equilibrium of displacement at the current temperature step through the iterative procedure (*e.g.,* using Newton's method). More effort is required to solve the equilibrium equation with the iterative method at each temperature step, but the implicit method enables a larger step size to be used due to higher numerical stability.

1.2 Tailored Response through Geometric Modulation of Actuator

Figure 1.1 shows a representative phase diagram of SMA material in the stress-temperature range. At zero stress, the martensite start temperature M_s and the martensite finish temperature M_f dictate the range and the direction of the forward transformation in which the SMA material transforms into the martensite phase. Analogously, the austenite start temperature A_s and the austenite finish temperature A_f dictate the range into the austenite phase through the reverse transformation. Transformation strains are generated when the SMA material is in the martensite phase and subsequently recovered after returning to the austenite phase. The stress influence coefficients of martensite C^M and of austenite C^A

denote respectively the slopes of forward and reverse transformation boundaries for applications with an applied load and hence nonzero stress. The phase diagrams for the three SMA materials adopted in the design process presented in this work are presented in Fig. 1.2. The commercially available SMA options employed in this work are the Flexinol® by Dynalloy, Inc. denoted by SMA 1 [58], SmarFlex® by SAES Getters denoted by SMA 2 [40], and another Flexinol® by Dynalloy, Inc. denoted by SMA 3 [54].

The hybrid SMA actuators modeled are fixed on one end with the other end attached to a structure in which their position is governed by the actuator motion. The actuators are composed of multiple wire section connected in series. Each wire section experiences equivalent force due to the applied load. However, the stress exerted upon the wire sections may differ due to different cross-sectional areas. A larger stress causes the transformation temperature ranges to shift to the right corresponding to the transformation boundaries depicted on the phase diagram. Thus, the stress can be adjusted for the individual wire sections through designating the proper cross-sectional area to obtain different transformation temperature ranges. In Fig. 1.3(a), a hybrid SMA actuator consisting of two wire sections with a single SMA material but different cross-sectional areas shows unique transformation temperature ranges relative to that for a single-section actuator of equal length. Figure 1.3(b) shows the standalone actuators composed with the same length and cross-sectional area for the three SMA materials, which have different transformation boundaries according to Fig. 1.2. In the same figure, the black curve showcases a global response of the hybrid SMA actuator that combines the three SMA materials through three discrete wire sections of the same cross-sectional area and section length while remaining geometrically equivalent to the standalone actuators. Thus, the objective of this work is to design SMA actuators through modulating the geometric configurations and SMA material options so that the sections transform at specific temperature ranges to obtain a global hysteretic response that approximates a target displacement vs. temperature actuation path.

1.3 Actuator Design Leveraging Machine Learning Techniques

As a high-speed computational approach, surrogate modeling enabled by machine learning represents an alternative approach to predict the actuation path with high accuracy while being less computationally intensive. In the second part of this work, a machine learning-assisted method is presented for modeling the actuator response of the SMA actuators. The machine learning method takes in a representative set of data and leverages pattern recognition on the influence of the design parameters to enable prediction of the actuation paths. This approach circumvents the need of going through the constitutive equations for every iteration at each temperature step. The structural model devised based on a constitutive SMA model does not guarantee convergence, in which convergence issues during the iterative process consume an extensive amount of computation time. Moreover, post-processing is required as it is needed to establish penalty criteria to omit the non-converged

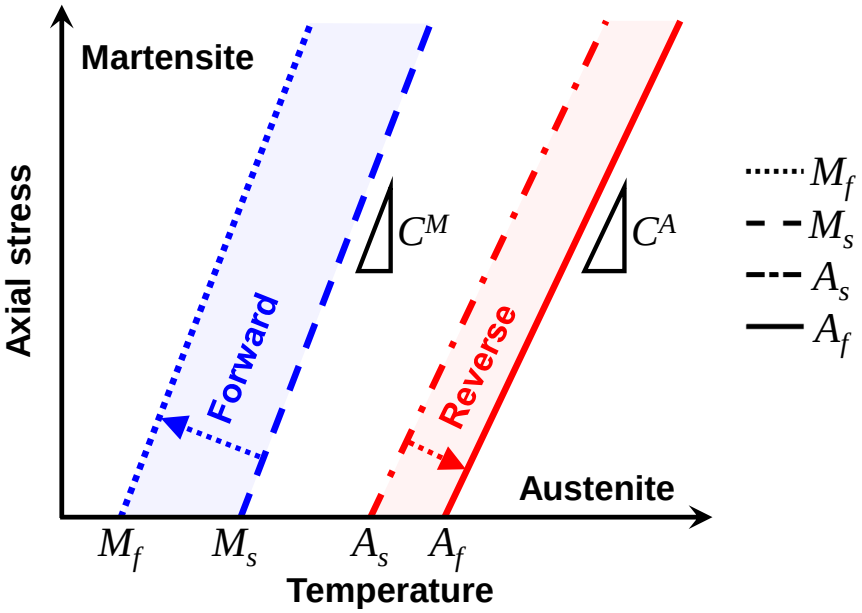

Figure 1.1: Phase diagram of SMAs showing transformation temperatures at zero stress (M_f, M_s, A_s, and A_f), stress influence coefficients (C^M and C^A), and bands for forward and reverse transformations.

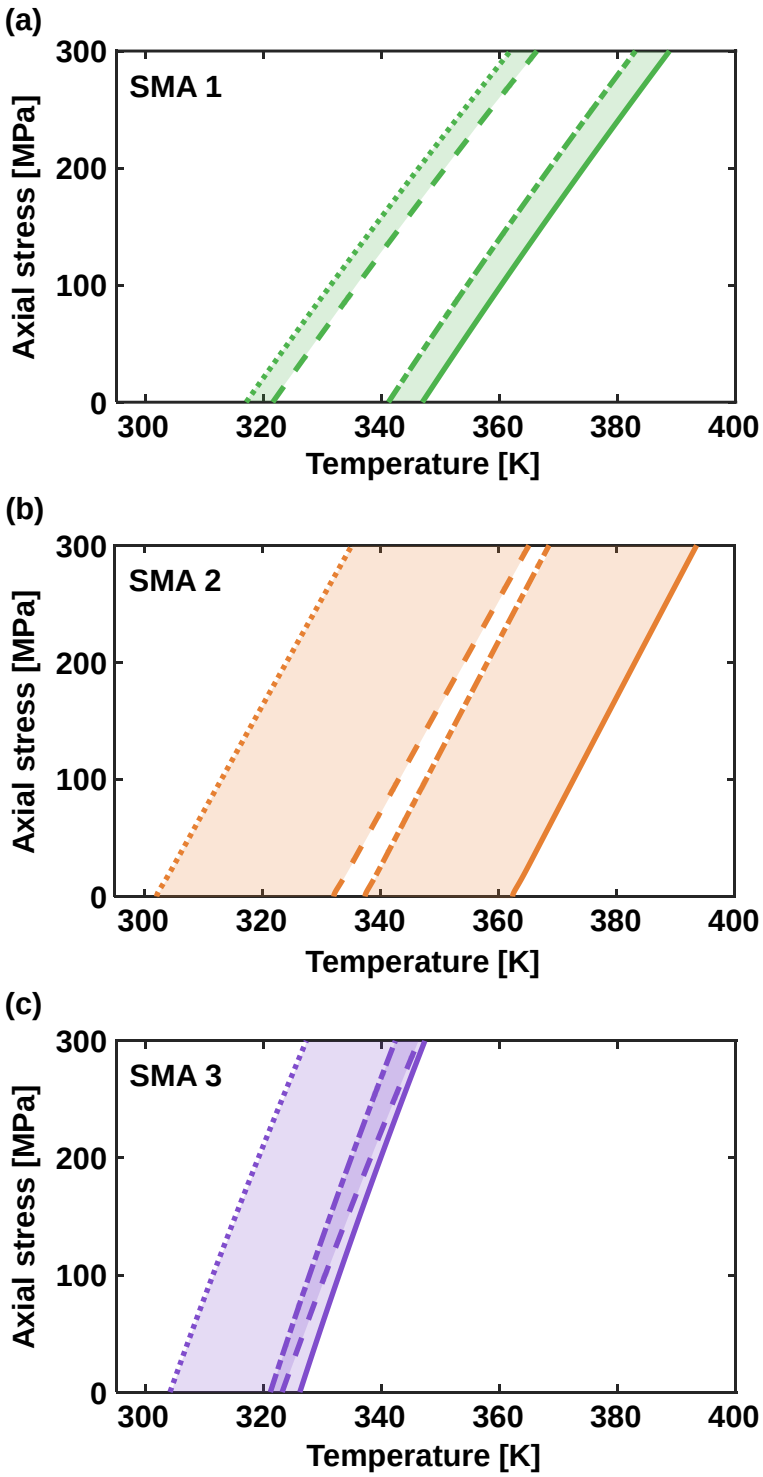

Figure 1.2: Phase diagrams for (a) SMA 1, (b) SMA 2, and (c) SMA 3. The parameters for these materials are obtained from Refs. [58, 40, 54], Respectively. Reprinted from [13].

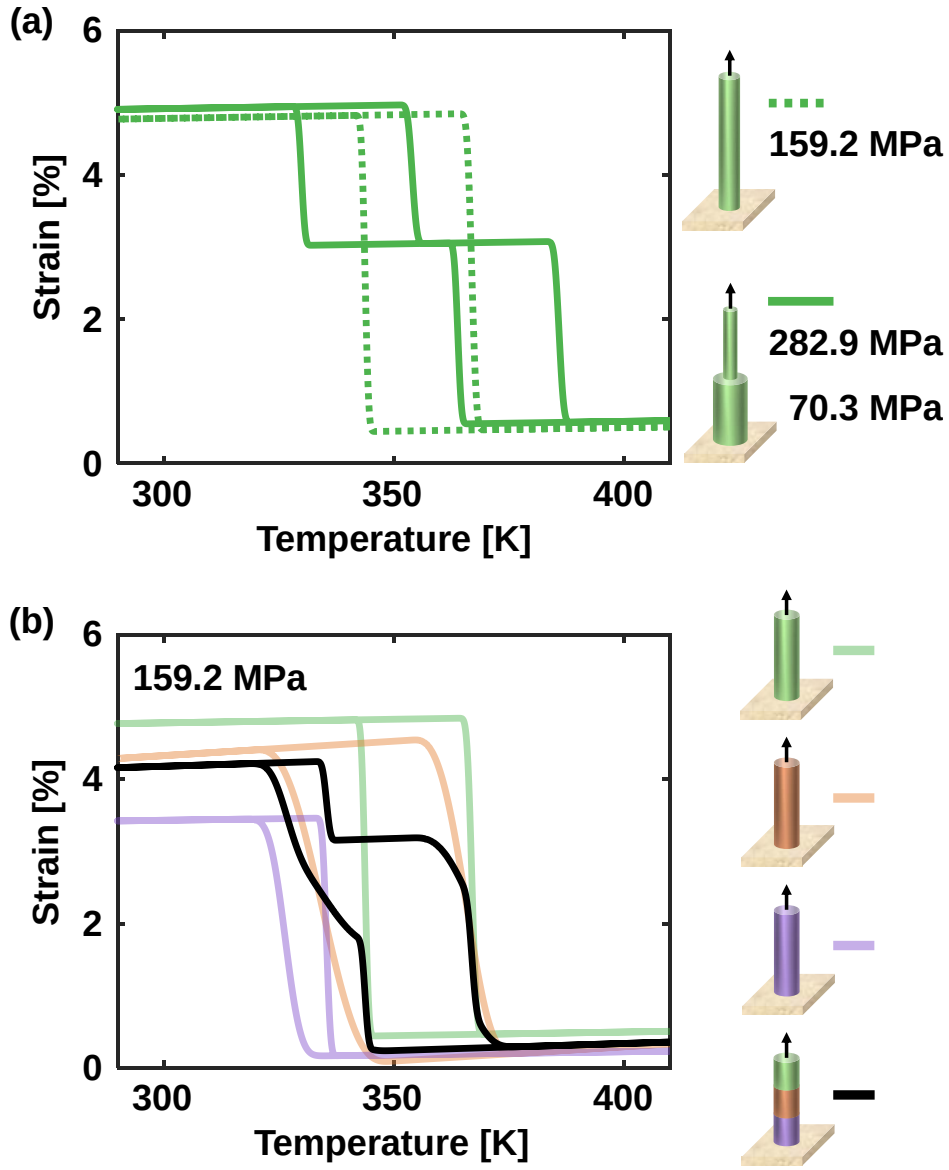

Figure 1.3: Comparison of the global actuation paths for single monolithic and hybrid SMA actuators demonstrating (a) the influence of geometric properties and (b) the influence of SMA selection. Reprinted from [13].

results from being taken into consideration for the subsequent optimization process. By forgoing the structural modeling approach, a solution (prediction) is guaranteed along with reduction in the computation time and effort without the iterative process accompanied by convergence issues. Machine learning has been applied to SMA applications before, but most work on SMAs that integrate machine learning methods focuses on the control aspect considering hysteretic effects rather than the characterization of the material response

[2, 25, 28]. Nevertheless, Valasek *et al.* presented the characterization of SMA behavior by implementing artificial neural network and reinforcement learning [18, 27]. Zhang and Xu demonstrated a low-cost option of using a Gaussian process regression model to determine the SMA transformation temperatures from various physical parameters [59]. Liu *et al.* used various machine learning models to study the correlation between the composition and the transformation temperatures [35].

In this work, a structural model is leveraged to generate a representative set of data for training a surrogate model via machine learning. Multiple sub-models are created corresponding to the different SMA materials employed. The Latin hypercube sampling method is implemented to generate 20000 design samples for each material combination, in which the strain vs. temperature data along with the minimum aspect ratio and maximum stress constraints are acquired. An ensemble regression model using decision trees with bootstrap aggregating is implemented due to its high model flexibility towards producing accurate predictions while being low on computer memory usage. The trained surrogate model enables the prediction of the actuation response of single-section actuators without the need of conventional structural simulations. The outputs of the individual actuator sections are subsequently evaluated collectively to obtain the global actuation response of the hybrid SMA actuators. The surrogate model is used as the design evaluator for the efficient design optimization of hybrid SMA actuators using genetic algorithm. The circumvention of using structural simulations during the optimization process enables the reduction of labor, time, and cost for the synthesis of hybrid SMA actuators for different smart systems.

1.4 Morphing Wing Enabled by Shape Memory Alloy Actuation

Novel and refined aerostructure designs with enhanced fuel efficiency and aerodynamic performance constitute a critical design requirement for the conception of next generation aircraft. Most aircraft employ wing designs that exhibit compromises due to the limitations of fixed wing shape geometry. The corresponding designs are tailored for a specific flight regime (*e.g.,* cruise) to provide the optimum performance. In normal working conditions, aircraft experience various phases of flight (*e.g.,* takeoff, climb, descend, and landing), such that non-idealized wing configurations introduce efficiency losses due to diminished performance [6, 31, 50]. Current aircraft incorporate discrete control surfaces (*e.g.,* flaps, ailerons, and rudders) to adjust the flight characteristics during flight. However, geometric discontinuities from conventional control surfaces generate additional aerodynamic drag and subsequently reduce the efficiency. The desire to mimic birds have always influenced the development of flight structures because they can adaptively change their wing shape based on flight conditions to maximize performance. Deriving from biomimicry, a morphing wing enables shape modulation during flight to adapt to different flight scenarios to improve both fuel economy and maneuverability. Morphing wing designs also preserve smoothness in the wing surface to minimize skin friction drag. Morphing wing designs encompass, but not limited to, span extension, camber variation, and spanwise twisting to adjust the aerodynamic characteristics [37]. Morphing wing designs with local and global morphing capabilities demonstrate predominant increased lift performance, enhanced flight stability, and reduced aerodynamic drag compared to conventional wings with fixed shapes [5, 53].

Due to the constrained space within the wing, bulky electric and hydraulic powered actuation systems are unattractive because they require complicated engineering effort to be accommodated into the wing structure and to ensure that they function properly [6, 32].

Smart materials such as SMAs have shown increased footprint in their implementation toward morphing wing design in recent years. Typical SMAs exhibit strain of up to 5% at their low-temperature martensite phase, and the strain is recoverable upon returning to their high-temperature austenite phase through heating. The shape memory effect enables SMA-based components to behave as both thermal sensors, actuators, and structural elements. The advantages of SMAs include being lightweight, compact, and actuation that are silent and free of debris [4, 16]. Altogether, the high actuation energy density enables SMAs to be excellent candidates for wing morphing applications. Leal *et al.* presented a morphing wing design with SMA actuator components embedded in the skin of the airfoil [32]. Saunders *et al.* fabricated a twisting wing that implements a SMA torque tube to provide spanwise twisting [48]. Nevertheless, designs that incorporate SMA-based components (*e.g.,* SMA skins and beams) require customized SMA designs that are expensive and require comprehensive material testing. Although shape memory alloy torque tubes present a simple design solution for wing morphing systems, their drawbacks include high production cost and slow actuation—making them inferior to SMA wire actuators. Among various designs reported in literature, two concepts were fabricated by Kang *et al.* [23] and Emiliavaca *et al.* [10] which featured camber morphing wings with configurable internal support structures enabled by SMA wires and springs.

The mass of wing morphing systems typically negates the efficiency advantages they bring to aircraft [48]. Current morphing wing designs that incorporate SMA wires or springs often require complex mechanisms to enable wing morphing. The implementation of tensegrity-based mechanism presents an alternative approach to designing lightweight wing morphing systems. Tensegrity structure consists of a structurally stabilized set of bodies (*e.g.,* rigid bodies and struts) that are connected to a network of tensile components. The modulation of the pre-stress or rest length of the tensile components enables change in the shape of the structure. A tensegrity structure also showcases high strength-to-weight ratio due to its load-bearing and energy absorption characteristics [11, 12, 51]. Henrickson *et al.* presented a

design technique to transform airfoil profiles via actuation of tensile components within the internal tensegrity structure [19]. Wing designs employing tensegrity principles demonstrate reduced weight compared to conventional wing structures with similar strength characteristics. Moreover, tensegrity systems do not compromise the structural integrity of the wing and other aircraft structures [55]. The aforementioned attractive properties of tensegrity structures, coupled with the actuation ability of SMAs, enable them to be applicable for morphing wing designs.

This part of the research investigates a novel twisting wing enabled by shape memory alloy wire actuation through an internal tensegrity mechanism. A full-span wing morphing methodology is presented by adapting the design by Skelton and de Oliveira on a tensegrity tower [52], which demonstrates a 40° relative rotational motion between the top and the bottom of the tower with their longitudinal distance fixed. This torsional mechanism is integrated along the wingspan as a cylindrical tensegrity column to enable spanwise twist. The presented design expands upon the work on a tensegrity twisting wing through the implementation of SMA wires into the tensegrity column as actuating members to facilitate wing morphing [41, 42]. Joule heating is used to increase the temperature of SMA wires to induce contraction in their length that subsequently produces twisting motion. The reversal of the SMA actuation to untwist the wing occurs as the SMA wires return to their initial length through convective cooling.

A previous design study demonstrates the capability of tensegrity twisting wing to undergo 19.5° twist [42], whereas wing morphing systems using typical SMA torque tubes only provide up to about 10° twist [48]. The incorporation of SMA wires into a tensegrity system reduces the manufacturing complexity and cost due to their wide accessibility and removes the need for customized SMA components. The use of commercially available SMA wires improves reliability and convenience without requiring comprehensive empirical testing to comprehend the material properties of new SMAs. The proposed lightweight and compact

wing morphing system through a tensegrity mechanism with SMA wires replaces conventional support structures and control surface actuation systems to potentially reduce the structural weight and provide more space for other systems and payload. Correspondingly, the implementation of a tensegrity mechanism enabled by SMA wire actuation for wing morphing can achieve the desired aerodynamic improvements due to the elimination of discrete control surfaces without compromises in weight. This research explores the feasibility of the SMA-enabled tensegrity twisting wing at the scale of a radio-controlled unmanned aerial vehicle (UAV). The UAV selected in this study is the Carl Goldberg Falcon Mark II UAV. This UAV is chosen for the high stall angle of attack of its airfoil (the angle of attack after which an airfoil exceeds its maximum lift coefficient and is prone to stalling), which enables higher twist angles to be achieved without stalling any section along the wing span. The component hierarchy of the SMA-enabled tensegrity twisting wing is illustrated in Fig. 1.4.

1.5 Summary of Contributions and Outline of the Thesis

In summary, the main research contributions of this work are:

i Devising a geometric approach towards designing SMA axial actuators to tailor their actuation responses

ii Modeling of the actuation response for multi-section SMA axial actuators through a reduced-order numerical model

iii Design study of the multi-section SMA actuators considering constraints and uncertainty analysis on the geometric and material parameters

iv Incorporation of machine learning techniques for the efficient surrogate modeling of the

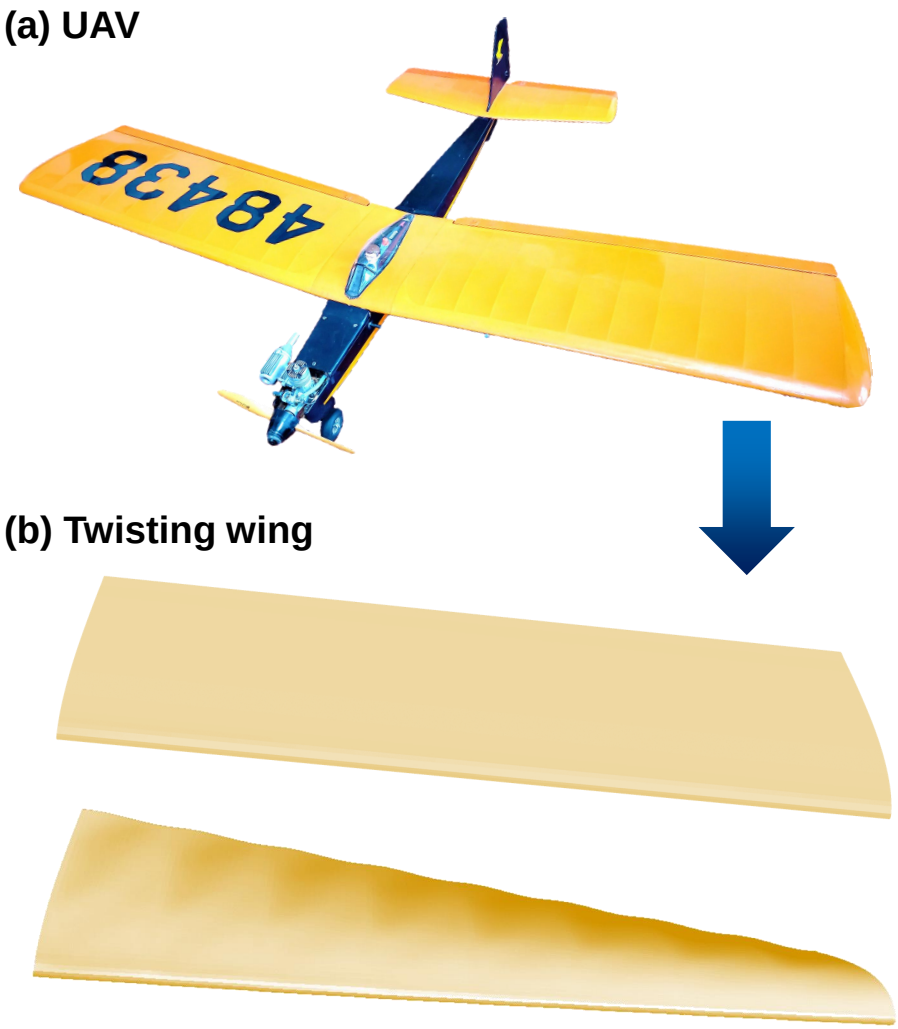
(a) UAV
48438
(b) Twisting wing

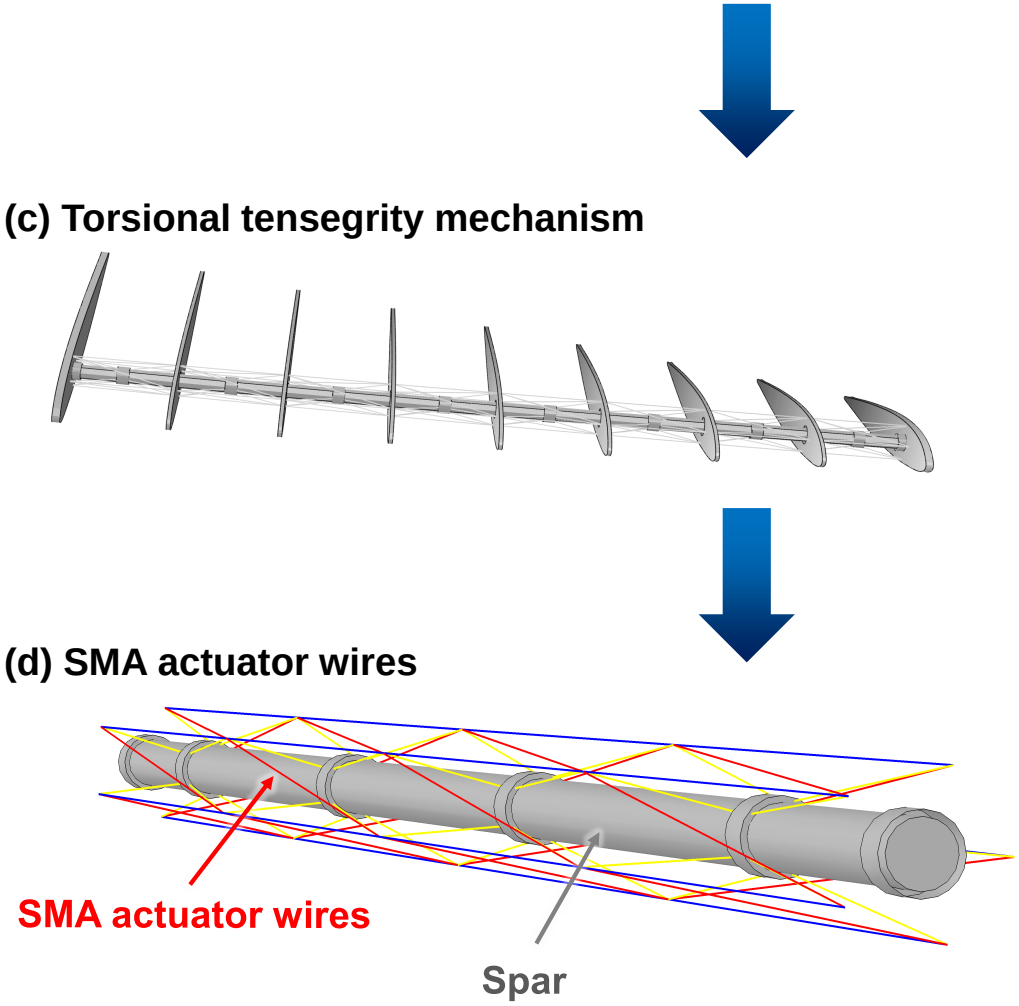

Figure 1.4: Component hierarchy of the SMA-enabled tensegrity twisting wing. (a) UAV, corresponding in this study to the Carl Goldberg Falcon Mark II UAV. (b) Replacement of a conventional wing by a twisting wing. (c) Torsional tensegrity mechanism that enables twisting motion. (d) SMA actuator wires that drive the torsional tensegrity mechanism. Adapted from [15].

actuator response and design optimization of hybrid SMA actuators.

v Exploration of a twisting wing with integrated internal torsional tensegrity mechanism enabled by SMA wire actuation through computational simulations and experimental validation

The remainder of this thesis is organized as follows: Chapter 2 details the modeling of multi-

section SMA axial actuators and their numerical implementation towards the modeling of their actuation response; Chapter 3 presents the uncertainty analysis and design study of the hybrid SMA actuators; Chapter 4 describes the implementation of surrogate models as the design evaluator for the efficient design optimization of hybrid SMA actuators circumventing structural simulations; Chapter 5 presents the design exploration and evaluation of leveraging SMA wire actuation to facilitate the facilitate an internal torsional tensegrity mechanism and hence enable twisting motion in a morphing wing; and Section 6 provides the conclusions and future works. A comprehensive list of symbols is provided in Appendix A.

Chapter 2

Multi-section Shape Memory Alloy Axial Actuators

[1] [2] This chapter provides an overview of the modeling of the hybrid SMA actuators that subsequently enables the implementation of numerical implementation of constitutive models for the evaluation of the actuation response. In Section 2.1, the geometric modeling of the hybrid SMA actuators through connecting multiple wire sections in-series is presented. Section 2.2 details the formulation of the reduced-order numerical model for the hybrid SMA actuators.

[1]Portions of this chapter are reprinted or adapted from [Weilin Guan and Edwin A. Peraza Hernandez, 2020, "Design framework for multi-section shape memory alloy axial actuators considering material and geometric uncertainties," Proceedings of the ASME 2020 International Design Engineering Technical Conferences and Computers and Information in Engineering Conference, DETC2020-22683. https://doi.org/10.1115/DETC2020-22683]. Figures and texts are reprinted by permission of the American Society of Mechanical Engineers.

[2]Portions of this chapter are reprinted or adapted from [Weilin Guan, Hasitha J. Hewakuruppu, and Edwin A. Peraza Hernandez, 2021, "Machine learning-assisted modeling and design optimization of hybrid shape memory alloy axial actuators," Proceedings of the ASME 2021 Conference on Smart Materials, Adaptive Structures and Intelligent Systems, SMASIS2021-68340. https://doi.org/10.1115/SMASIS2021-68340]. Figures and texts are reprinted by permission of the American Society of Mechanical Engineers.

2.1 Axial Actuator Model

The longitudinal direction of the actuator is designated as the x-direction in which cross-sectional areas and material options constitute two design parameters of the hybrid SMA actuators. The section length constitutes a design parameter in which the length for sections ($n > 1$) are expressed in terms of the section length ratio ϕ.

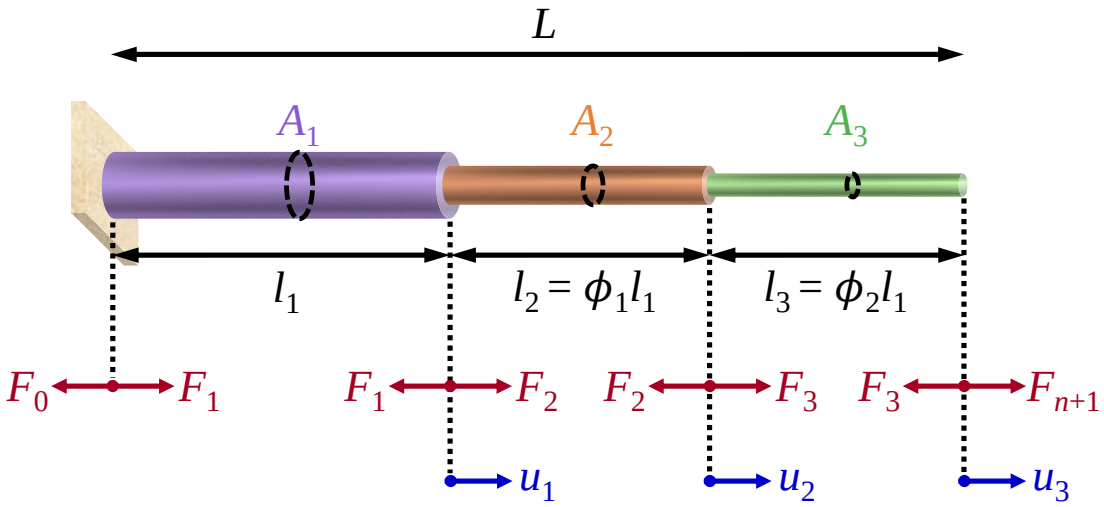

Figure 2.1: Schematic of a hybrid SMA actuator showing force balance, nodal displacements, section lengths, and cross-sectional areas. Reprinted from [13].

The number of wire sections in the actuator is denoted by n, and there is a total of $n + 1$ nodes denoting the end points of the actuator and the connections between the sections. The 0^{th} node is located at the fixed end of the actuator. The distance at the i^{th} node from the 0^{th} node is represented by x_i. The section length l_i is the difference between the nodal points at the ends of the corresponding section with $l_i = x_i - x_{i-1},\ i \in \{1, \ldots, n\}$.

The total actuator length L, illustrated in Fig. 2.1, is assumed as a design parameter. Therefore, the *section length ratios* (ϕ_j), $j \in \{1, \ldots, n-1\}$, which are the ratios between l_{j+1} and l_1, are used in lieu of the section lengths l_i directly as the design parameters, The total length

of the actuator is then given by:

$$L \;=\; l_1 + \sum_{j=1}^{n-1} \phi_j l_1 \;=\; l_1 \left(1 + \sum_{j=1}^{n-1} \phi_j \right), \tag{2.1}$$

which can be modified to acquire the length of the first section in terms of L and the section length ratios:

$$l_1 = \frac{L}{\left(1 + \sum_{j=1}^{n-1} \phi_j\right)}. \tag{2.2}$$

The section lengths for the remaining sections are then determined with the section length ratios defined as follows:

$$l_{j+1} = \phi_j l_1. \tag{2.3}$$

2.2 Numerical Implementation

The nodal displacements u_i, $i \in \{0, \ldots, n\}$, and the section lengths l_i calculated from Eq. (2.3) are then used to compute the strain at each section:

$$\varepsilon_i = \frac{u_i - u_{i-1}}{l_i} \qquad i \in \{1, \ldots, n\}. \tag{2.4}$$

The constitutive SMA model by Lagoudas *et al.* provided in Ref. [30] is then implemented to compute the stresses σ_i by using the strains ε_i from Eq. (2.4) and the SMA material parameters. The *cross-sectional areas* of the different wire sections forming the actuators A_i, $i \in \{1, \ldots, n\}$, are imposed as the design variable for the actuator besides the section length ratios ϕ_j. The wire actuators investigated in this work consist of circular actuator

cross-sections, where the cross-sectional areas ($A_i = \pi r_i^2$) are determined using the radius of each section. The force of each section is then obtained by multiplying the stresses σ_i with the cross-sectional areas as shown:

$$F_i = \sigma_i A_i. \tag{2.5}$$

There is an externally pulling force ($F_{n+1} = k_0$) applied at the non-constrained n^{th} end node, where k_0 is a constant applied force representing the case investigated in this work. After determining the forces at each actuator section, force equilibrium at each nodal point is checked via the residual vector $\mathbf{R} \in \mathbb{R}^n$ defined as follows:

$$R_i = F_{i+1} - F_i. \tag{2.6}$$

If the norm of the vector $\mathbf{R}$ is smaller than a set tolerance, it is assumed that force equilibrium is satisfied. Otherwise, the vector of nodal displacements $\mathbf{u} \in \mathbb{R}^n$ vector is iteratively recomputed until the norm of $\mathbf{R}$ decreases below the tolerance. The Newton's method is employed to compute a new $\mathbf{u}$. This requires determining the derivative of residual vector with respect to the nodal displacements ($\frac{\mathrm{d}\mathbf{R}}{\mathrm{d}\mathbf{u}} \in \mathbb{R}^{n \times n}$). The derivatives of the force equilibrium equations with respect to the displacements at each section and its adjacent sections populate each respective column in the $\frac{\mathrm{d}\mathbf{R}}{\mathrm{d}\mathbf{u}}$ matrix as follows:

$$\frac{\mathrm{d}R_i}{\mathrm{d}u_{i-1}} = -\frac{\mathrm{d}F_i}{\mathrm{d}u_{i-1}}, \quad \frac{\mathrm{d}R_i}{\mathrm{d}u_i} = \frac{\mathrm{d}F_{i+1}}{\mathrm{d}u_i} - \frac{\mathrm{d}F_i}{\mathrm{d}u_i}, \quad \frac{\mathrm{d}R_i}{\mathrm{d}u_{i+1}} = \frac{\mathrm{d}F_{i+1}}{\mathrm{d}u_{i+1}}. \tag{2.7}$$

Using Eqs. (2.4) and (2.5), the derivative of F_i with respect to u_i and u_{i-1} is given by:

$$\frac{\mathrm{d}F_i}{\mathrm{d}u_i} = \frac{A_i}{l_i}\frac{\mathrm{d}\sigma_i}{\mathrm{d}\varepsilon_i}, \qquad \frac{\mathrm{d}F_i}{\mathrm{d}u_{i-1}} = -\frac{A_i}{l_i}\frac{\mathrm{d}\sigma_i}{\mathrm{d}\varepsilon_i}. \tag{2.8}$$

The matrix $\frac{\mathrm{d}\mathbf{R}}{\mathrm{d}\mathbf{u}}$ has the following structure:

$$\frac{\mathrm{d}\mathbf{R}}{\mathrm{d}\mathbf{u}} = \begin{bmatrix} \frac{\mathrm{d}R_1}{\mathrm{d}u_1} & \frac{\mathrm{d}R_1}{\mathrm{d}u_2} & 0 & \dots & & \\ \frac{\mathrm{d}R_2}{\mathrm{d}u_1} & \frac{\mathrm{d}R_2}{\mathrm{d}u_2} & \frac{\mathrm{d}R_2}{\mathrm{d}u_3} & 0 & \dots & \\ 0 & \frac{\mathrm{d}R_3}{\mathrm{d}u_2} & \frac{\mathrm{d}R_3}{\mathrm{d}u_3} & \frac{\mathrm{d}R_3}{\mathrm{d}u_4} & 0 & \dots \\ \vdots & \vdots & \vdots & & \ddots & \\ & & & & \frac{\mathrm{d}R_n}{\mathrm{d}u_{n-1}} & \frac{\mathrm{d}R_n}{\mathrm{d}u_n} \end{bmatrix}. \tag{2.9}$$

The Newton's Method is applied to compute the new displacement vector $\mathbf{u}_{\text{new}}$ as follows:

$$\Delta\mathbf{u} = -\left(\frac{\mathrm{d}\mathbf{R}}{\mathrm{d}\mathbf{u}}\right)^{-1}\mathbf{R}, \tag{2.10}$$

where $\mathbf{u}_{\text{new}}$ is calculated by adding $\Delta\mathbf{u}$ from Eq. (2.10) and the current displacement vector $\mathbf{u}_{\text{cur}}$:

$$\mathbf{u}_{\text{new}} = \mathbf{u}_{\text{cur}} + \Delta\mathbf{u}. \tag{2.11}$$

The calculations in Eqs. (2.10)-(2.11) are repeated until the norm of $\mathbf{R}$ decreases below the designated tolerance value. Another method used for checking convergence is to inspect if $\frac{\|\Delta\mathbf{u}\|}{L}$ is below a tolerance value. The process described in this section is repeated each the temperature step. The complete process is implemented herein in `Matlab`®.

Chapter 3

Hybrid Shape Memory Alloy Actuators

[1] After establishing the SMA model for the design evaluation of actuation response, this chapter proceeds to study the effectiveness in modulating the geometric configurations of the hybrid SMA actuators to obtain customized response compared to a target actuation path. Section 3.1 details an uncertainty analysis on the geometric and material parameters considering their respective constraint. A design of experiment study performed on different combinations of actuator geometric design parameters is presented in Section 3.2

[1]Portions of this chapter are reprinted or adapted from [Weilin Guan and Edwin A. Peraza Hernandez, 2020, "Design framework for multi-section shape memory alloy axial actuators considering material and geometric uncertainties," Proceedings of the ASME 2020 International Design Engineering Technical Conferences and Computers and Information in Engineering Conference, DETC2020-22683. https://doi.org/10.1115/DETC2020-22683]. Figures and texts are reprinted by permission of the American Society of Mechanical Engineers.

3.1 Design Evaluation

The SMA material parameters assumed in this work are based on the data provided in Ref. [40] that studied the design and optimization of SMA-based structures and are provided in Table 3.1. The Young's modulus of austenite and martensite are denoted by E^A and E^M, respectively. The minimum transformation strain of the SMA, $H_{\min}$, is implemented alongside its maximum value, H_{sat}, to define the magnitude of the transformation strain of the SMA, where the influence of the stress on the magnitude of the transformation strain is defined by the transformation strain parameter k [30]. The hardening exponents n_1, n_2, n_3, n_4 govern the smoothness of the transitions between thermoelastic and transformation regimes. The transition between the SMA and thermoelastic transformations is sharp if $n_i = 1$ and the transition curvature increases as n_i decreases. Lastly, the thermoelastic expansion coefficient α^{th} determines the slope of the thermoelastic transformation.

Table 3.1: Material properties for the SMA model [40].

Material parameter	**Average value**	**Standard deviation**
H_{sat}	0.044	0.00010
$H_{\min}$	0	N/A
E^A	48000 MPa	50 MPa
E^M	42900 MPa	50 MPa
k	0.24	0.005
A_s	337.4 K	0.50 K
A_f	362.4 K	0.50 K
M_s	332.1 K	0.50 K
M_f	302.1 K	0.50 K
C^A	9.54 MPa/K	0.0050 MPa/K
C^M	9.0 MPa/K	0.0050 MPa/K
α^{th}	4×10^{-5} K^{-1}	8×10^{-7} K^{-1}
n_1	0.3	0.005
n_2	0.34	0.005
n_3	0.2	0.005
n_4	0.34	0.005

In general, the SMA parameters are not deterministic and may exhibit variations from sample to sample [39], which makes it imperative to consider such variations when designing robust

SMA actuators. Therefore, uncertainty of the material parameters is accounted for within the design framework presented in this work. A sampling-based method is employed to perform uncertainty analysis, where the material and geometric parameters of the considered actuators are given as normal distributions. The standard deviations of the material parameters are provided in Table 3.1. For each studied design, a set of q_s samples are analyzed where the geometric parameters for each sample are determined from their normal distributions. The designated set of q_s random samples is generated through the `Matlab`® built-in Latin hypercube sampling function `lhsdesign`. The number of samples, q_s, designated for the uncertainty analysis in this work is 100.

Since the axial SMA actuators studied in this work are based on commercially available options, the uncertainty analysis also considers manufacturing specifications. Shape memory alloy wire sections with four different actuator cross-sectional radii are considered in this work. The average values of the radii and their associated standard deviations are provided in Table 3.2.

Table 3.2: Cross-sectional radii considered for the SMA actuators.

Average radius	**Standard deviation**
0.15 mm	0.005 mm
0.20 mm	0.005 mm
0.25 mm	0.005 mm
0.30 mm	0.005 mm

A target displacement vs. temperature path is assumed for optimization, and the discrepancy between this target path and actual path of the actuator represents the quantity to minimize. The specific responses used to quantify the discrepancy between target and actual paths are illustrated in Fig. 3.1. The displacement at the n^{th} node u_n is compared to the target displacement u_{tar} indicated by the target path for each temperature step to obtain the displacement error at each temperature step as follows:

$$e_{\text{T}} = \left| u_{\text{tar}} - u_n \right|, \tag{3.1}$$

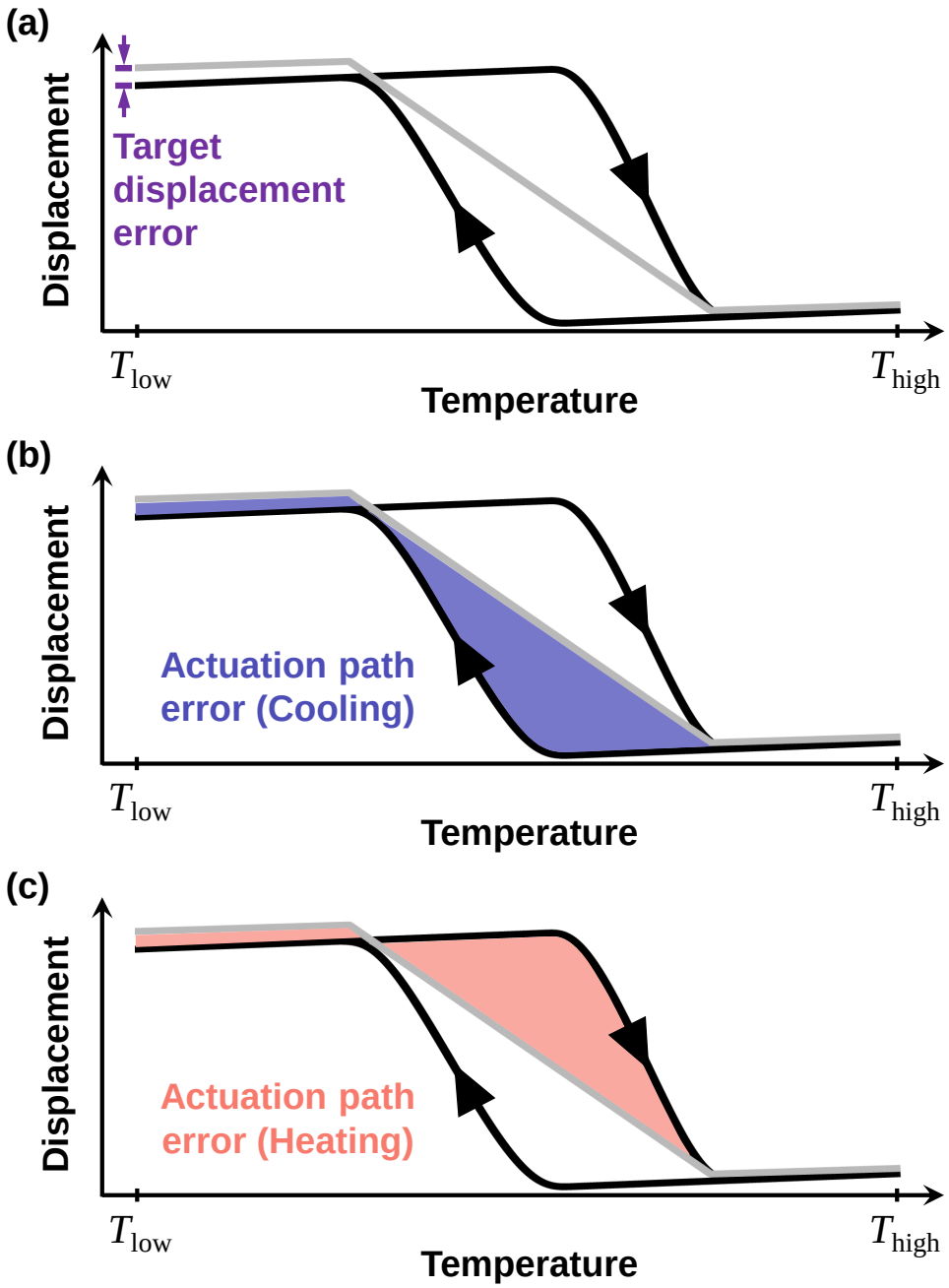

Figure 3.1: Schematics of the three actuation path errors used to evaluate the actuator design: (a) target displacement error; (b) actuation path error for cooling; and (c) actuation path error for heating. Reprinted from [13].

The difference in area between the actual and target actuation paths is denoted by e_u. The trapezoidal rule is used to compute the area difference between the actual and target actuation paths (see Figs. 3.1(b) and 3.1(c)) as follows:

$$e_u = \sum_{r=2}^{s} \left| \frac{T_r - T_{r-1}}{2} \right| (e_{T,r} + e_{T,r-1}) \,, \tag{3.2}$$

where s^{th} is the number of temperature steps. A second displacement error is implemented to penalize designs that do not achieve the desired maximum displacement at T_{low}. This error is shown schematically in Fig. 3.1(a). The target displacement error, defined as the squared difference between the actual and target displacements at T_{low}, is evaluated as:

$$e_{\Delta u} = \left(u_{\text{tar}}(T_{\text{low}}) - u_n(T_{\text{low}})\right)^2 . \tag{3.3}$$

The *actuation path error* (e) consists of sum of e_u from Eq. (3.2) and $e_{\Delta u}$ from Eq. (3.3). The target displacement error is multiplied by a factor $\lambda_{\Delta u}$ to obtain a comparable order of magnitudes between the two aforementioned error components:

$$e = e_u + \lambda_{\Delta u} e_{\Delta u}. \tag{3.4}$$

Figure 3.1 illustrates the two error categories for each iteration. For each temperature step u_n is compared with u_{tar}, and the shaded areas in between represents the shape function displacement error. The shaded areas in Figs. 3.1(b) and 3.1(c) show the total shape function displacement error for cooling and heating, respectively. Figure 3.1(a) shows the target displacement error, the difference in the displacement between the shape function and that of the actuator at T_{low}.

Two failure criteria are implemented towards the design study to avoid results that violate the physical assumptions of the model. No section in the actuator should exceed the maximum stress of the SMA material or contain a low length-to-diameter aspect ratio. Stress failure

is assumed when one or more of the total q_s samples exceeds the maximum stress limit σ^* provided in Table 3.3.

The aspect ratio of a wire section in the actuator, defined as its length divided by its diameter, should be greater than the designated minimum aspect ratio AR^* provided in Table 3.3. This criterion is required because wire sections of low aspect ratios violate the model assumption that these sections behave as one-dimensional members. The aspect ratio of the i^{th} wire section is given as follows:

$$AR_i = \frac{l_i}{2r_i}. \tag{3.5}$$

Just as with the stress criteria, a design is deemed as unfeasible if any of the wire sections of its q_s samples violates the aspect ratio constraint.

Table 3.3: Input parameters considered in the design study.

Parameter	**Value**	**Parameter**	**Value**
T_{low}	200 K	T_{high}	500 K
L	20 mm	$u_{\text{tar}}(T_{\text{low}})$	0.85 mm
k_0	30 N	q_s	100
σ^*	500 MPa	AR^*	10
$\lambda_{\Delta u}$	8		

In the simulation process for each sample of an actuator design, the temperature of the actuator is initiated at T_{high} where the SMA is at the austenite phase. The first half of the simulation involves decreasing the temperature in multiple steps until reaching T_{low}. During the process, the SMA transforms into the martensite phase. The temperature of the actuator is subsequently increased from T_{low} to T_{high} for the second half of the simulation. An adaptive temperature step method is implemented to facilitate the simulation process. The default step size used for the analysis is 1 K, and the algorithm automatically reduces the step size by half when convergence for the residual vector fails.

3.2 Design of Experiments

For the examples provided here, a refined design of experiments (DOE) study is performed and the most favorable actuator design is determined as that design from the DOE with the minimum actuation path error e averaged over all its samples. The simulations are executed with the different combinations of actuator design parameters consisting of four different cross-sectional radii (Table 3.2) and a range of section length ratios. The results obtained are then used to compute the actuation path error e for each sample using Eq. (3.4), along with the stress and aspect ratio failure criteria. The design objective function, where the cross-sectional area and length ratio for each wire section of the actuator are the design variables, is stated as follows:

$$\begin{aligned} \text{Find:} \quad & A_i,\ \phi_j \\ \text{That minimize:} \quad & \text{avg}_l(e) \\ \text{Subject to:} \quad & \max_l(\sigma_i) < \sigma^*, \quad \min_l(AR_i) > AR^* \\ & i \in \{1, 2, \ldots, n\}, \quad j \in \{1, 2, \ldots, n-1\} \\ & l \in \{1, 2, \ldots, q\}. \end{aligned} \tag{3.6}$$

Designs with a single wire section ($n = 1$), two wire sections ($n = 2$), and three wire sections ($n = 3$) are evaluated in this example. The results showed that the addition of sections decreases the average actuation path error $\text{avg}_l(e)$. Thus, for the sake of brevity, the results for the axial actuators with $n = 1$ and $n = 2$ are omitted. Figure 3.2 shows contour plots of average actuation path error in the design space defined by the section length ratios ϕ_1 vs. ϕ_2 for actuators with three wire sections ($n = 3$). The four contour plots shown in Figure 3.2 correspond to the four combinations of wire section radii for actuators with $n = 3$. The shaded areas in the contour plots represent the unfeasible designs due to violation of the

maximum stress or the minimum aspect ratio failure criteria. Each point on the contour plots represents the error of an actuator design defined by ϕ_1 and ϕ_2.

After performing the simulations on the different actuator section configurations through a range of section length ratios for single, two, and three sections, the most favorable design resulted from a 3-section actuator with section radii 0.15 mm, 0.20 mm, and 0.30 mm. The corresponding design is schematically indicated with the star label in Fig. 3.2(b). The average actuation path error $\text{avg}_l(e)$ for this design is 11.9393. Overall, the results show that combining multiple wire sections in a single SMA axial actuator improves the performance by allowing the actuators to reach an actuator path closer to the target.

The geometry of the most favorable axial SMA actuator design is shown in Fig. 3.3. The first section has a radius of $r_1 = 0.15$ mm and a section length of $l_1 = 8.040$ mm, the second section has a radius of $r_2 = 0.20$ mm a section length of $l_2 = 4.254$ mm ($\phi_1 = 0.5291$), and the third section has a radius of $r_3 = 0.30$ mm a section length of $l_3 = 7.706$ mm ($\phi_2 = 0.9585$). The corresponding displacement vs. temperature plot depicting the actuation path during the cooling and heating cycles for this actuator is shown in Fig. 3.4.

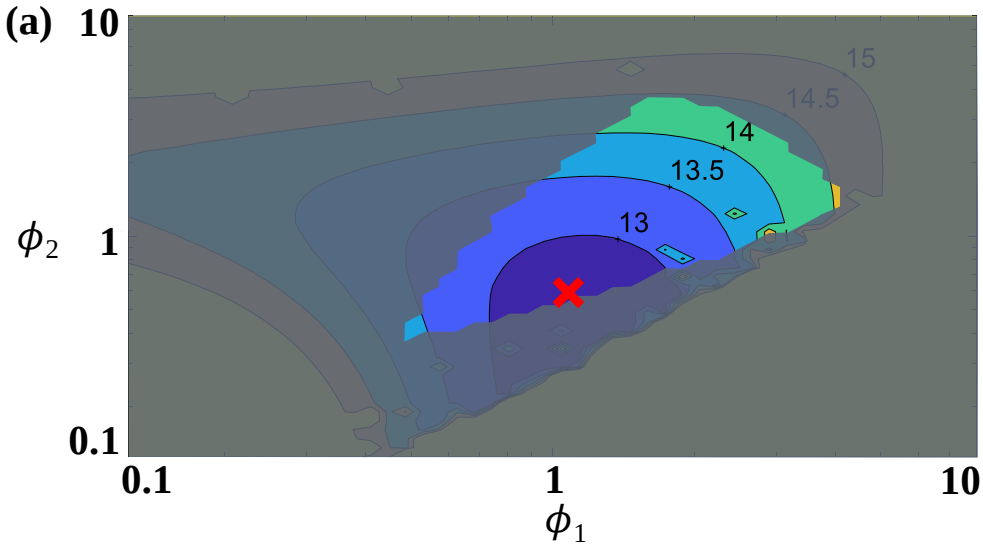
(a)
10
15
14.5
14
13.5
13
ϕ_2
1
0.1
0.1
1
10
ϕ_1

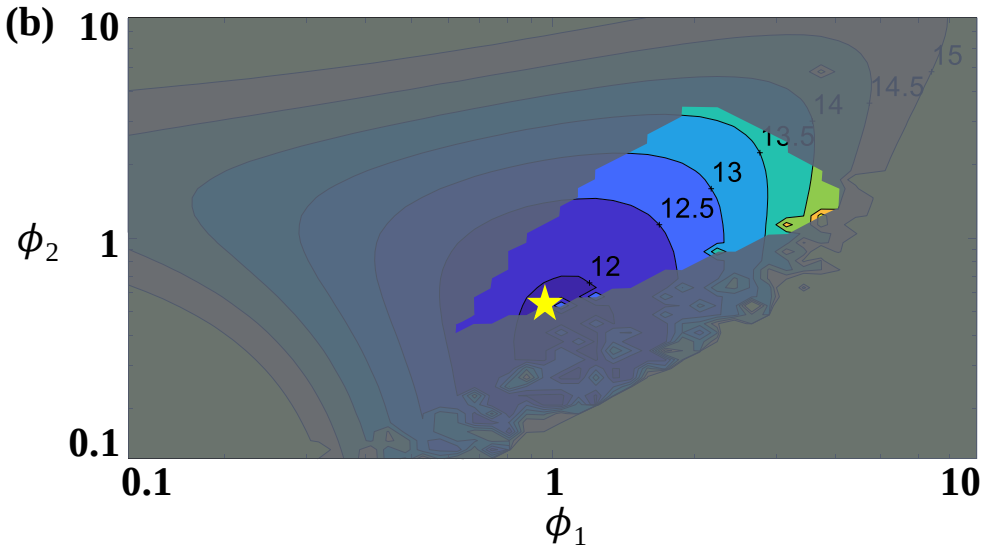
(b)
10
15
14.5
14
13.5
13
12.5
12
ϕ_2
1
0.1
0.1
1
10
ϕ_1

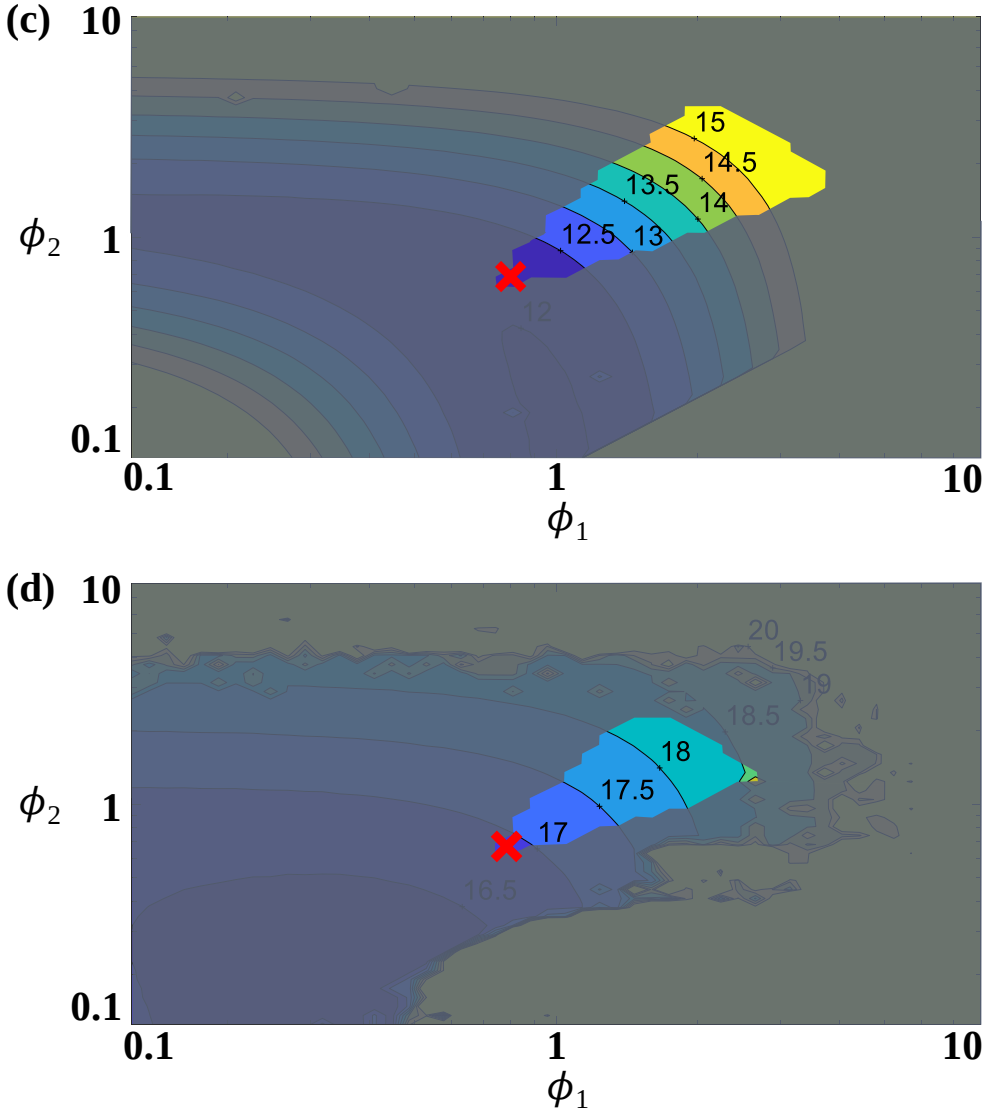

Figure 3.2: Contour plots of average actuation path error e for an SMA actuator with three sections. The design space is defined by the section length ratios ϕ_1 and ϕ_2. The darker region indicates unfeasible designs as assessed by the considered failure criteria. The radii of the three sections in the actuators for each contour plot is as follows: (a) 0.15 mm, 0.20 mm, 0.25 mm; (b) 0.15 mm, 0.20 mm, 0.30 mm; (c) 0.15 mm, 0.25 mm, 0.30 mm; and (d) 0.20 mm, 0.25 mm, 0.30 mm. The crosses and the star indicate the feasible designs with the minimum average actuation path error for each plot, and the star denotes the lowest among them. Adapted from [14].

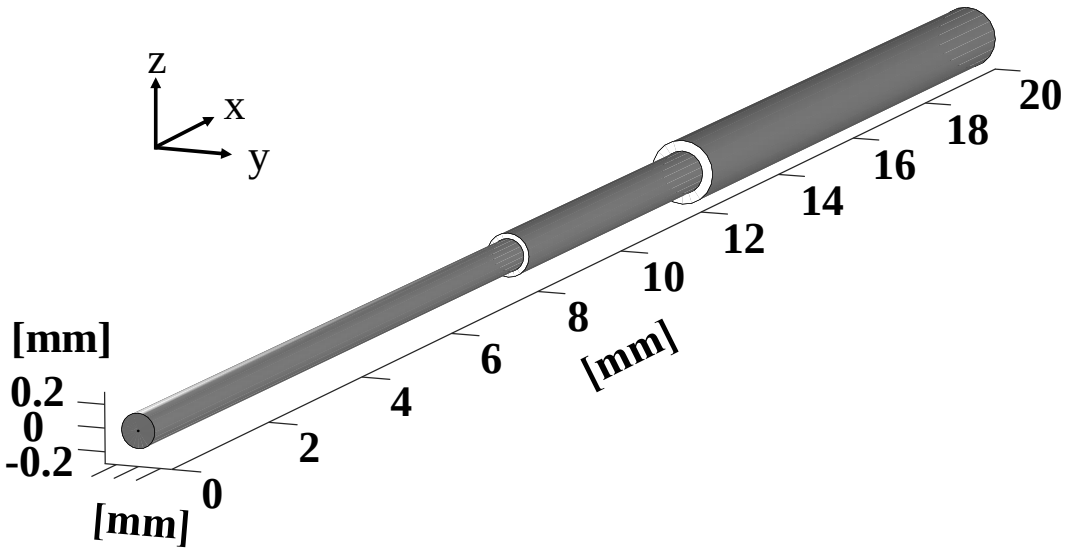

Figure 3.3: Geometry of the most favorable axial actuator design indicated in Fig. 3.2(b). The radii of the wire sections are 0.15 mm, 0.20 mm, 0.30 mm, from left to right. Reprinted from [13].

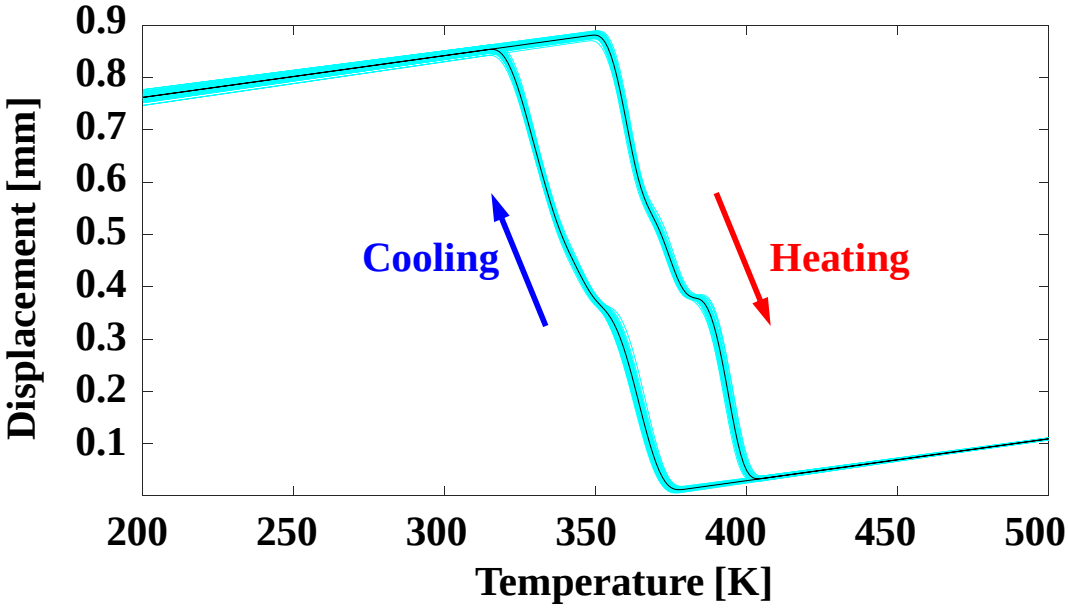

Figure 3.4: Displacement vs. temperature actuation path of the most favorable actuator design indicated in Fig. 3.2(b). The black curve represents the average path and the blue region represents the collection of the paths determined from the sampling evaluations. Reprinted from [13].

Chapter 4

Machine Learning-assisted Modeling

[1] After the design of experiment study that demonstrates the capability of geometric modulation of hybrid SMA actuators to tailor their response, an efficient machine learning-assisted approach is leveraged to enhance the design optimization process of the hybrid SMA actuators. Section 4.1 details the training of the surrogate models and correspondingly their validation against the structural models. Section 4.2 shows the design optimization of hybrid SMA actuators using the trained surrogate models.

4.1 Surrogate Model Training and Validation

A trained surrogate model based on an ensemble of binary decision trees is leveraged for the design evaluation of hybrid SMA actuators. The numerical analysis through the structural model in Ref. [30] outputs the stress-temperature data while taking the strain-temperature

[1]Portions of this chapter are reprinted or adapted from [Weilin Guan, Hasitha J. Hewakuruppu, and Edwin A. Peraza Hernandez, 2021, "Machine learning-assisted modeling and design optimization of hybrid shape memory alloy axial actuators," Proceedings of the ASME 2021 Conference on Smart Materials, Adaptive Structures and Intelligent Systems, SMASIS2021-68340. https://doi.org/10.1115/SMASIS2021-68340]. Figures and texts are reprinted by permission of the American Society of Mechanical Engineers.

data. The data are then iterated through Newton's Method until convergence of the force equilibrium to obtain the final strain outputs. The surrogate model aims to characterize the SMA actuation response through circumventing the iterative process through the implementation of the constitutive SMA model. The input space includes the cross-sectional area defining a single-section actuator, the operating temperature range for actuation, and the applied force polynomial coefficients. The outputs include the strain at each temperature step, maximum stress, and the minimum aspect ratio. The response of each actuator section is obtained individually using the surrogate model and evaluated to obtain the global response of the hybrid SMA actuator. The strain outputs are scaled to their respective section length and summed to obtain the global actuation displacement. The maximum stress and minimum aspect ratio out of all the actuator sections constitute the global maximum stress and minimum aspect ratio, respectively. The trained surrogate model subsequently enables the design evaluation of hybrid SMA actuators with different numbers of actuator sections.

A minimum temperature T_{low} of 290 K and a maximum temperature of T_{high} of 410 K are assumed during the cooling and heating cycles. A temperature increment of 0.01 K is used for heating and cooling to determine the corresponding actuation strain for obtaining the samples using the structural model. It has been shown that a larger temperature increment leads to convergence errors and faulty actuation paths. Subsequently, the strain outputs at 0.5 K temperature increments are mapped to the actuator design parameters. Table 4.1 provides the bounds and type for each of the design parameters considered during training. In this work, hybrid SMA actuators of two sections are considered, and a representative set consisting of 20000 design samples is generated for each of the six material combinations for the model training process. There are three different trained sub-models corresponding to the three commercially available SMA material options implemented. The SMA material for each section is denoted by the variable SMA_i in Table 4.1 and the material parameters for each SMA material option are provided in Table 4.2. These parameters are associated with the model described in Ref. [30]. The trained model is then validated using 5000 design

samples obtained from both the structural model and the surrogate model. The evaluation time for validation using the trained surrogate model is less than 8 minutes, whereas the evaluation time using structural simulations is 59 minutes. As shown in Figs. 4.1 and 4.2, the surrogate model demonstrates R^2 values of 0.99983 and 0.99979 for heating and cooling, respectively.

Table 4.1: Design variables considered in model training and design optimization, and their lower bound, upper bound, type, and discrete step.

Variable	**Lower bound**	**Upper bound**	**Type**	**Step**
SMA_i	1	3	Discrete	1
r_i	0.05 mm	0.25 mm	Continuous	-
k_0	1 N	2 N	Continuous	-

Table 4.2: Material properties for the SMA materials: SMA 1 [58], SMA 2 [40], SMA 3 [54]. The material properties are associated with the model presented in Ref. [30]. Values labeled with an * are estimated.

Material parameter	**SMA 1**	**SMA 2**	**SMA 3**
E^A	31500 MPa	48000 MPa	69000 MPa
E^M	20000 MPa	42900 MPa	30000 MPa
α^{th}	1×10^{-5} K^{-1} *	4×10^{-5} K^{-1}	8.8×10^{-6} K^{-1}
A_s	341.15 K	337.40 K	321.15 K
A_f	346.90 K	362.40 K	326.15 K
M_s	321.55 K	332.10 K	323.15 K
M_f	317.05 K	302.10 K	304.15 K
C^A	6.73 MPa/K	9.54 MPa/K	13.0 MPa/K
C^M	6.32 MPa/K	9.00 MPa/K	12.0 MPa/K
H_{sat}	0.041	0.044	0.030
H_{min}	0.041 *	0	0.030 *
k	-	0.24 MPa^{-1}	-
σ_{crit}	-	0	-
n_1	0.20 *	0.30	0.20 *
n_2	0.20 *	0.34	0.20 *
n_3	0.20 *	0.20	0.20 *
n_4	0.20 *	0.34	0.20 *

The design samples are trained using various regression models including linear regression, support vector machines (SVM), and decision trees. Linear regression models are not suitable

for this application due to the nonlinear relationship among the SMA parameters. SVM is not preferred as it has the longest training time compared to other models due to the large data set while not yielding substantial improvement in the accuracy. The ensemble of decision trees compensates the deficient accuracy using an independent decision tree model, and it yields short training time. Bootstrap aggregation is implemented due to the high dimensionality of the data set. The high model flexibility also enables the high prediction accuracy of the trained model.

4.2 Actuation Path Optimization

The design objective function is stated as follows:

$$
\begin{aligned}
\text{Find:} \quad & \text{SMA}_i,\ r_i,\ \phi_j,\ L \\
\text{That minimize:} \quad & e \\
\text{Subject to:} \quad & \sigma_i < \sigma^*, \quad AR_i > AR^*, \\
& \phi_{\text{L}} \leq \phi_j \leq \phi_{\text{U}}, \quad L_{\text{L}} \leq L \leq L_{\text{U}}, \\
& \text{SMA}_i \text{ and } r_i \text{ bounded as per Table 4.1} \\
& i \in \{1, 2, \ldots, n\}, \quad j \in \{1, 2, \ldots, n-1\},
\end{aligned}
\tag{4.1}
$$

where $\phi_{\text{L}} = 0.125$ and $L_{\text{L}} = 100$ mm are the corresponding values for the lower bounds and $\phi_{\text{U}} = 8$ and $L_{\text{U}} = 200$ mm are the corresponding values for the upper bounds.

Sample results of the implementation of the framework for the problem formulated in Eq. (4.1) are provided in Figs. 4.3(a) and 4.3(b), which respectively depicting the localized linear target path and the linear target path. A constant force k_0 of 1.2 N is assumed for both cases. Optimization is performed using the calibrated surrogate model to obtain

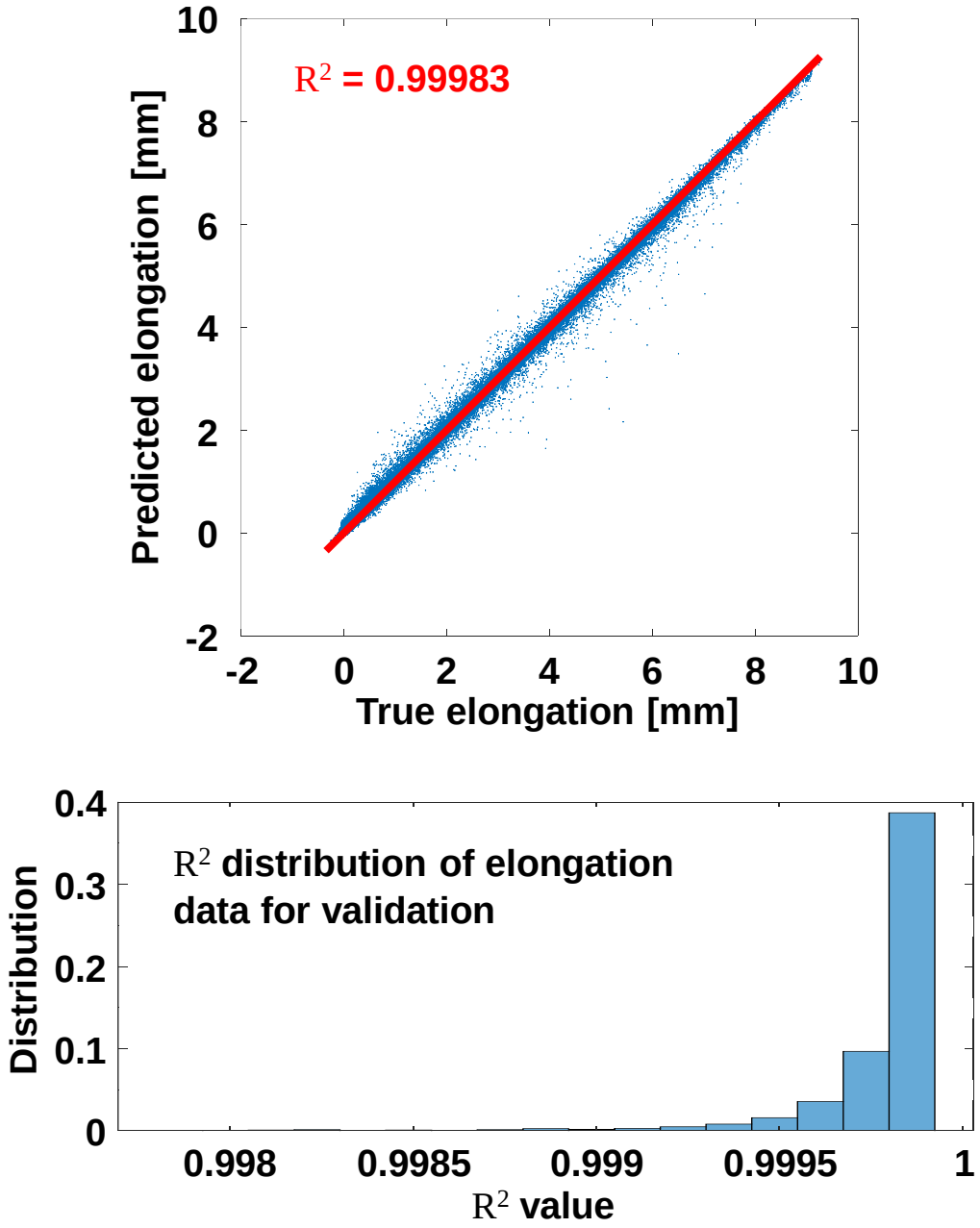

Figure 4.1: Parity plot and histogram for validation of the actuator displacements predicted by the surrogate model during heating. The Parity plot shows the average R^2 value for all 5000 samples while the histogram considers the individual R^2 values for each sample.

the actuation paths showed by the dashed curves, which possess fair closeness to their respective target path. The actuation path errors are $e = 72.4$ for the localized linear case in Fig. 4.3(a) and $e = 234.3$ for the linear case in Fig. 4.3(b). The actuator geometries and

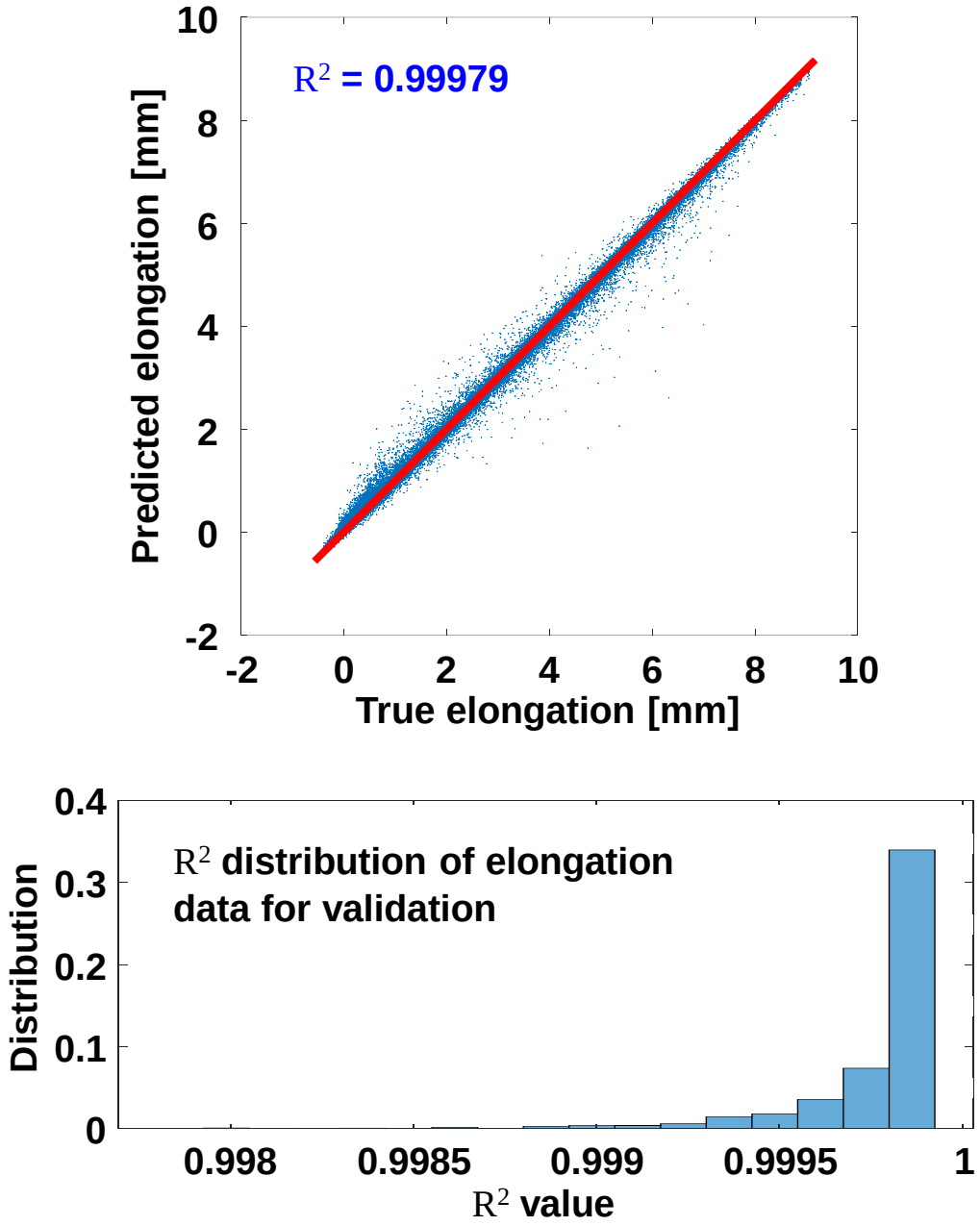

Figure 4.2: Parity plot and histogram for validation of the actuator displacements predicted by the surrogate model during cooling. The Parity plot shows the average R^2 value for all 5000 samples while the histogram considers the individual R^2 values for each sample.

materials obtained during the optimization process are also provided, where the diameter of the actuators is scaled by 50×. Both sections of the actuator are composed by SMA 3 for the case in Fig. 4.3(a), whereas the two sections of the actuator are formed by SMA 1 and SMA

3 for the case in Fig. 4.3(b). The results from optimization are verified by simulating the actuator with the optimal design parameters using the structural model. Both Figs. 4.3(a) and 4.3(b) show a good agreement between the actuation paths obtained from the surrogate and structural models. For the case in Fig. 4.3(b), a slight discrepancy is observed at the end of actuation during heating, which suggests that the surrogate model could be further improved by either using a higher number of samples for training, or exploration of other formulations.

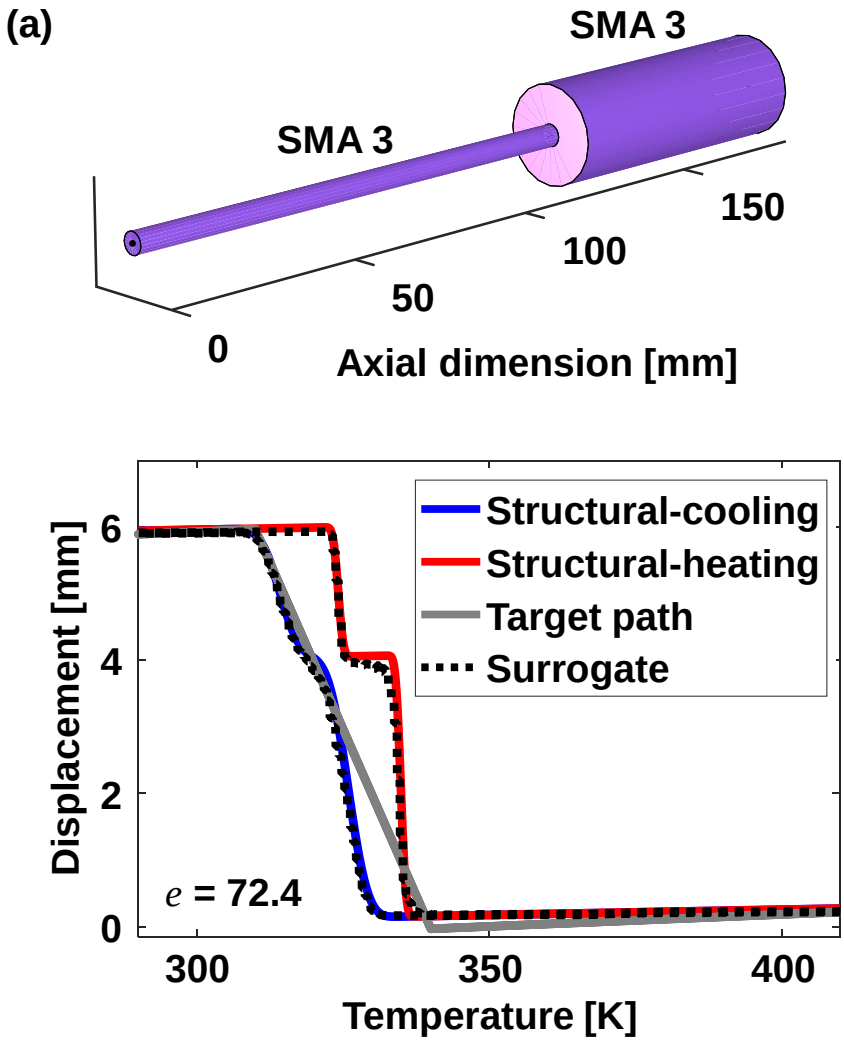

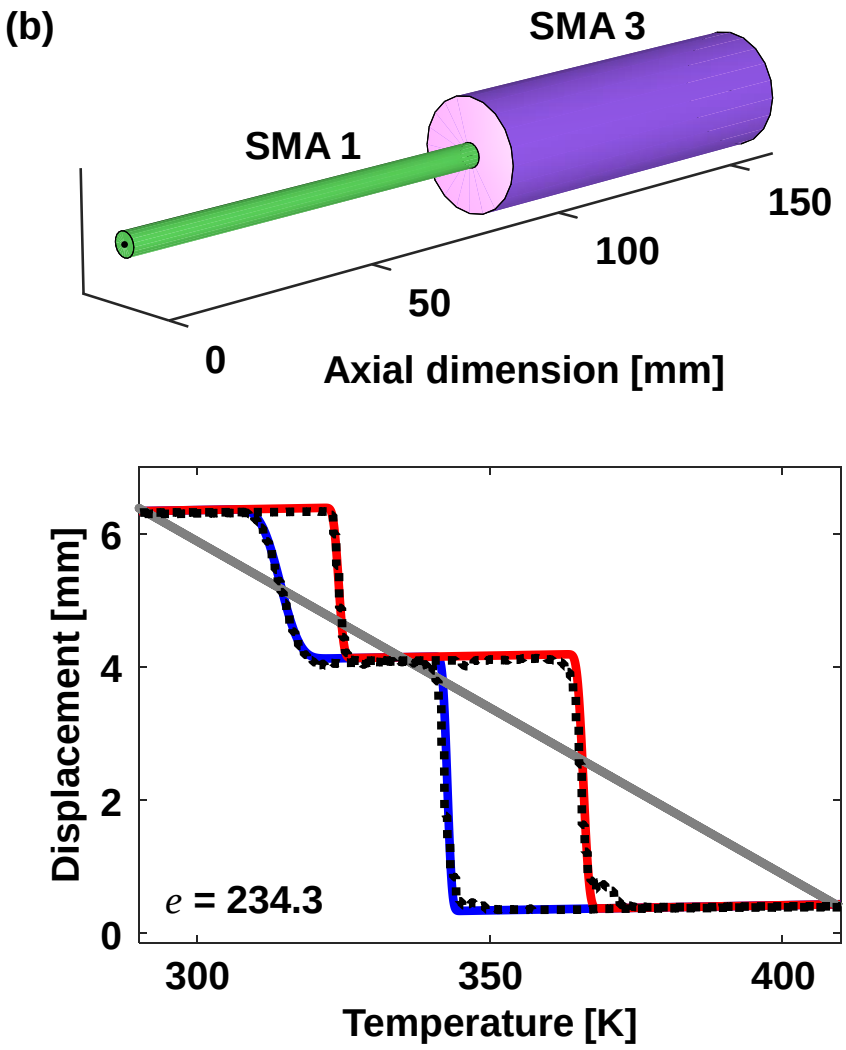

Figure 4.3: Results for the sample actuator design problems with (a) localized linear and (b) linear target paths. The obtained actuators are shown schematically with 50× scaled diameter. Adapted from [13].

Chapter 5

Tensegrity Twisting Wing

[1] This chapter focuses on the application of SMA axial actuators to facilitate a novel morphing wing design. Section 5.1 introduces the novel twisting wing with integrated torsional tensegrity mechanism, its aerodynamic characteristics compared to a convectional wing with control surfaces. Subsequently, Section 5.2 presents the implementation of SMAs into the tensegrity column to facilitate twisting, the experimental evaluation, finite element model created to evaluate the wing performance, and a design of experiment study.

5.1 Torsional Tensegrity Mechanism Design

The twisting wing provides global morphing through spanwise torsional deformation. This unibody design approach circumvents discrete control surfaces by adopting a smooth and continuous wing surface, which lowers aerodynamic drag. A trailing flap in conventional

[1]Portions of this chapter are reprinted or adapted from [Weilin Guan, Nguyen K. Pham, and Edwin A. Peraza Hernandez, 2021, "Design exploration of a tensegrity twisting wing enabled by shape memory alloy wire actuation," Proceedings of SPIE Smart Structures/NDE 2021, Active and Passive Smart Structures and Integrated Systems XV, 1158809, virtual conference. https://doi.org/10.1117/12.2582829]. Figures are reprinted by permission of the American Institute of Aeronautics and Astronautics, Inc.

wing designs, including that on the Carl Goldberg Falcon UAV, represents a discrete component that introduces a gap at its attachment to the primary wing body. To enable torsional deformation, the wing tip rotates about the spar formed by the internal tensegrity column relative to the wing root. Research on wing twisting by Philips *et al.* showed that the capability to adjust the twisting during flight reduces drag for improved aerodynamic efficiency [44]. Vos *et al.* demonstrated a twisting wing design by incorporating a threaded rod that rotates to twist the wing through induced skin warping deformation [57]. The warp-controlled wing exhibited sufficient gain in roll control over conventional wing designs. Rodrigue *et al.* explored a twist morphing wing using SMA wire actuation by crisscrossing two sets of SMA wires that go from the leading edge to the trailing edge and vice versa across the wingspan [46]. The respective results showed a substantial 13% increase in the lift-to-drag ratio.

Previous work demonstrated that for two wings with the same planform geometry, a twisting wing with smooth surface exhibits higher lift-to-drag ratio compared to a conventional wing with a trailing flap [41, 42]. In this work, the proposed tensegrity twisting wing concept leverages the wing profile of the Carl Goldberg Falcon Mark II UAV. The Carl Goldberg Falcon wing represents a design of the conventional wings due to the implementation of discrete control surfaces. Accordingly, the differences in aerodynamic performance between the Carl Goldberg Falcon wing with a trailing flap and the twisting wing adaptation are evaluated through CFD analyses. The configurations of the referenced wing with a trailing flap and the twisting wing adaptation are shown through the computational models in Figs. 5.1(a) and 5.1(b), respectively. For both models, the angle of attack α defines the angle between the airflow direction and the chord line at the wing root. The flap deflection angle δ defines the angle of the trailing flap in reference to the chord line at the wing root for the conventional wing. Analogously, the twist angle Φ defines the angle between the chord line at the wing root and that at the wing tip for the twisting wing. The computational models with the defined geometry are subsequently imported into `ANSYS`$^{\text{TM}}$ to perform CFD analyses.

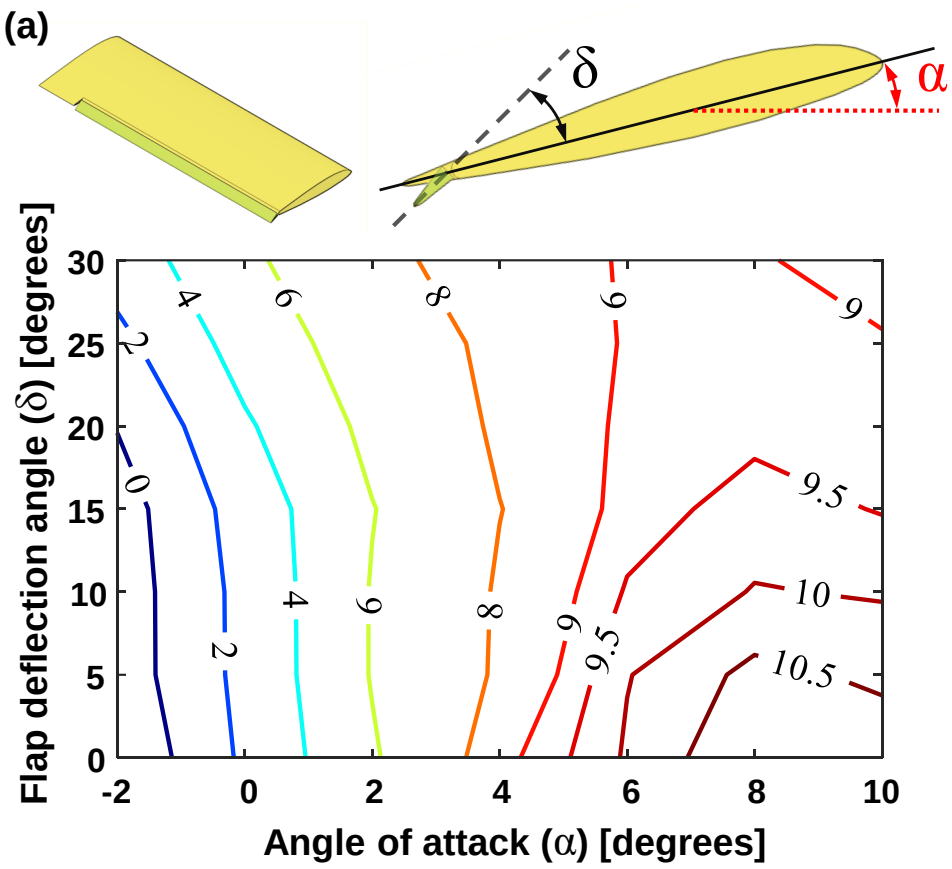
(a)
δ
α
Flap deflection angle (δ) [degrees]
Angle of attack (α) [degrees]
30
25
20
15
10
5
0
-2
0
2
4
6
8
10
0
2
4
6
8
9
9.5
10
10.5

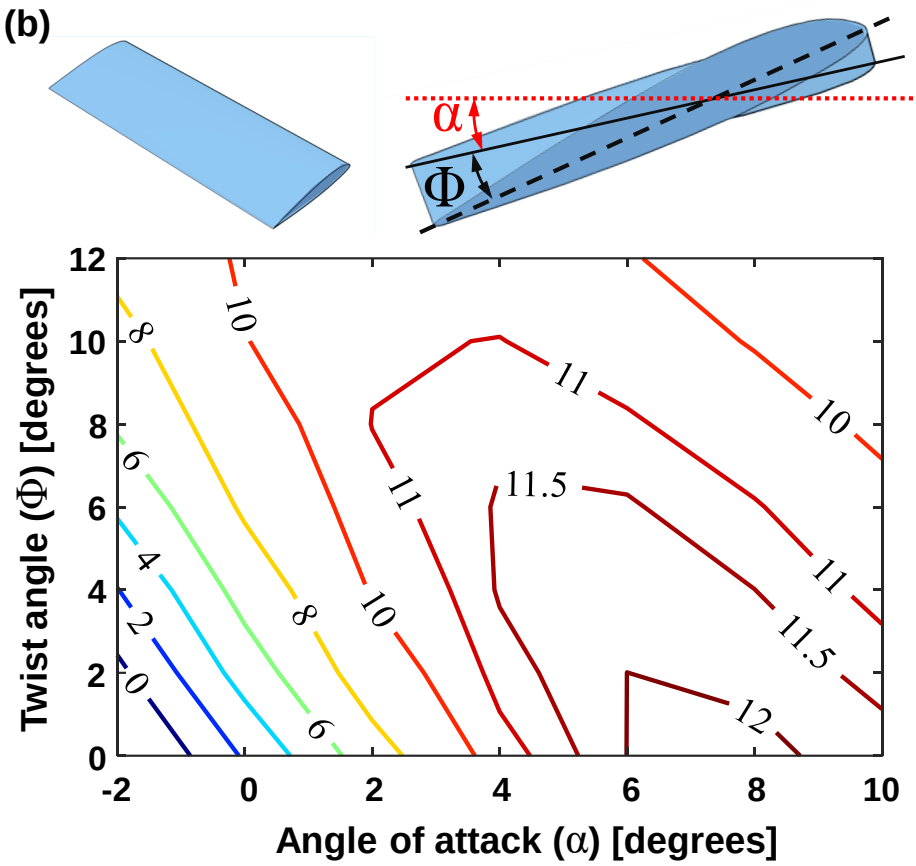

Figure 5.1: Comparative aerodynamic efficiency analysis of a twisting wing and a conventional wing. (a) Schematic of a conventional wing with a flap control surface indicating the *flap deflection angle* (δ) and *angle of attack* (α). The corresponding lift-to-drag ratio C_L/C_D contour plot is provided. (b) Schematic of a twisting wing showing *twist angle* (Φ) and α. The associated lift-to-drag ratio C_L/C_D contour plot is also shown. Adapted from [15].

Practical flight conditions are considered to determine attainable performance superiority of the twisting wing. The simulation for each model assumes an airflow speed of 20 m/s, which correlates to the typical cruising speed of the Falcon UAV. The angle of attack α is designated to be -2° to 10°. For the conventional wing case, the flap deflection angle δ is varied from 0° to 35°. For the twisting wing, the twist angle Φ ranges from 0° to 12°. The lift and drag coefficients (C_L and C_D, respectively) are the main output variables from the CFD analyses. The obtained results are shown via the lift-to-drag-ratio C_L/C_D to highlight the aerodynamic efficiency characteristic. Figure 5.1(a) shows the C_L/C_D contour as a function of δ and α for the conventional wing. Similarly, Fig. 5.1(b) shows the C_L/C_D contour as

a function of Φ and α for the twisting wing. Accordingly, the contour plots demonstrate higher lift-to-drag ratios for the twisting wing over the conventional wing within the studied range for α to constitute a more aerodynamically efficient design.

To leverage the improved aerodynamic performance demonstrated by using control surface-free twisting, an internal torsional mechanism inspired by the tensegrity tower design [52] is implemented to enable spanwise wing twisting motion. The torsional tensegrity mechanism incorporates a cylindrical spar that is oriented in the spanwise direction from the wing root to the wing tip. The ribs are laid out equidistantly in the spanwise direction. The region between each pair of ribs is denoted here as a tensegrity cell. The fixed spar travels through a circular hole within each rib, and the structure is designed such that the center of torsion coincides with the spar. A network of wires is placed within each tensegrity cell in a uniform circular pattern surrounding the spar. The wires comprise the tensile components of the tensegrity structure and allow for control of the twisting motion the ribs.

Figure 5.2(a) shows a simplified view of the torsional mechanism within each tensegrity cell, where only the connection points of the ribs with the actuator and longitudinal wires (which provide a bias restoring force) are shown. The contraction of the actuator wires generates a torque that twists the torsional mechanism, where this motion is obtained by rotating each pair of adjacent ribs relative to one another. The tensegrity cell with the entire set of its components is shown in Fig. 5.2(b). When the actuator wires are contracted, the longitudinal wires that are initially aligned along the span direction stretch and generate an opposing torque. Resembling a spring system, the tensegrity column returns to its initial configuration once the actuator wires are relaxed and returned to their initial length.

A coordinate system with the x-direction pointing towards chord direction from the leading to the trailing edge and the z-direction pointing along in the spanwise direction from root to tip is used to define the wire positions. The origin of the coordinate system is located in the center of the face of the spar at the root of the wing. Figure 5.3 shows a tensegrity

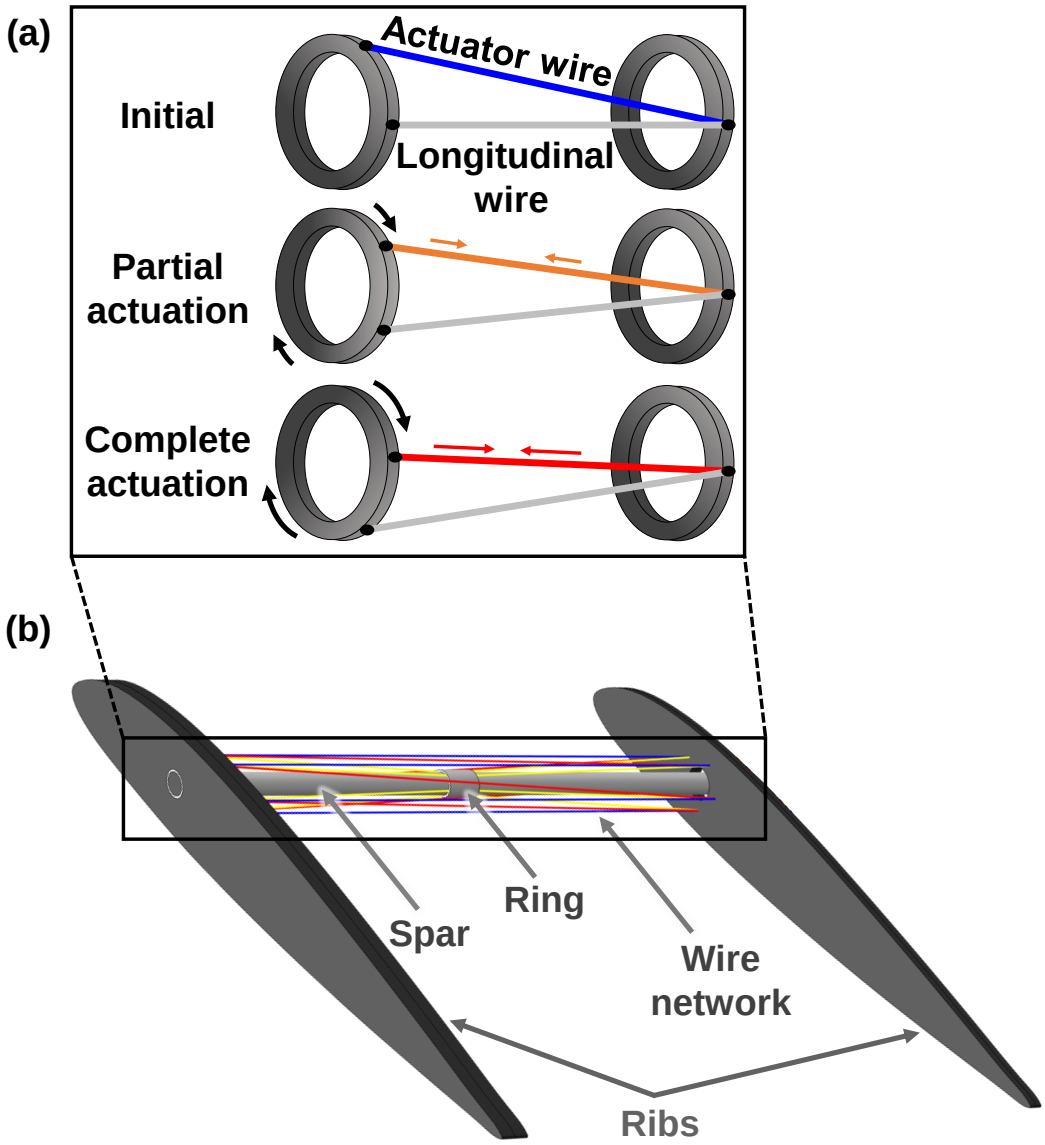

Figure 5.2: Torsional tensegrity mechanism. (a) Simplified schematic of a cylindrical cell exhibiting torsional motion enabled by contraction of an actuator wire. (b) Corresponding placement of the cell within the tensegrity twisting wing. Adapted from [15].

cell along with the coordinate system, associated dimensions, and points used to define the end points of each wire in the torsional tensegrity mechanism. The tensegrity wing design has two topological parameters corresponding to the *number of cells* (n_c) and the *number of wire sets* (n_w). Both n_c and n_w are considered in the DOE presented in Section 5.2. Each set of wires is composed of one actuator wire, one longitudinal wire, and two stabilizer wires.

Examples showing wing designs with 4, 6, and 8 cells and a single cell with different numbers of wire sets are shown in Figs. 5.4 and 5.5, respectively.

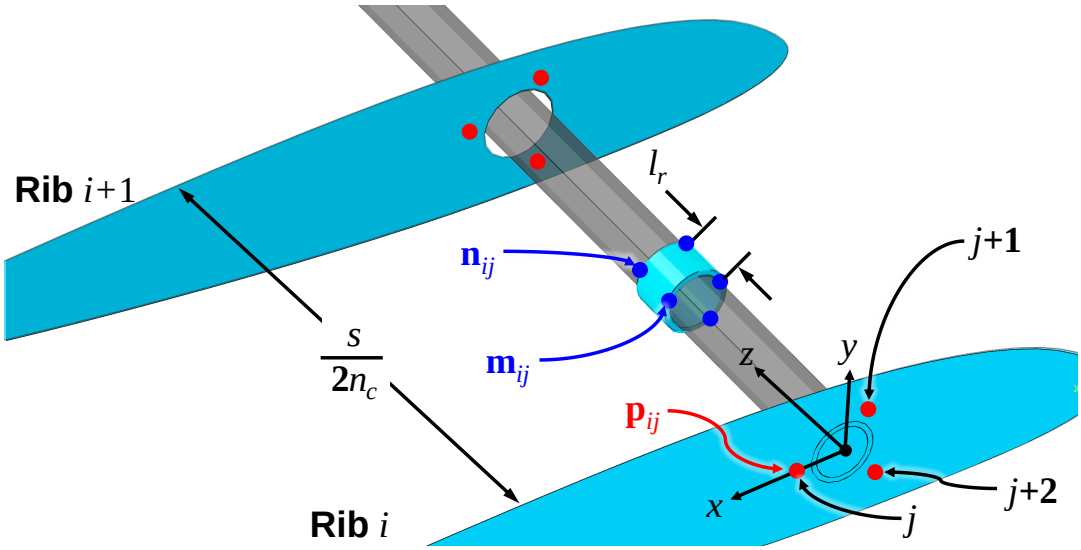

Figure 5.3: Schematic showing index convention and wire end points $\mathbf{n}_{ij}$, $\mathbf{m}_{ij}$, and $\mathbf{p}_{ij}$. The rib number and the wire set number are represented by the indices i and j, respectively. Reprinted from [15].

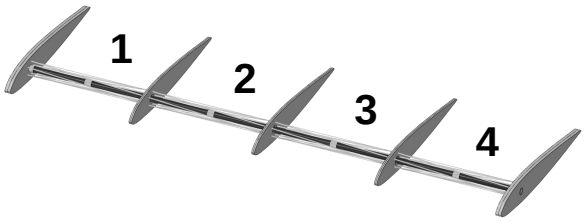

(a) 4 cells, $n_c = 4$.

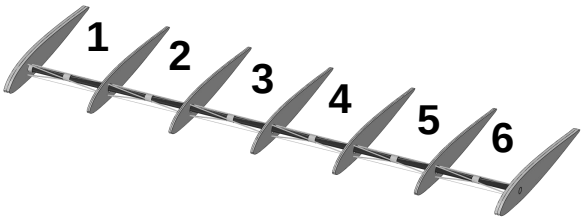

(b) 6 cells, $n_c = 6$.

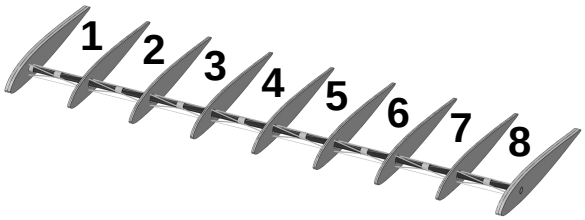

(c) 8 cells, $n_c = 8$.

Figure 5.4: Torsional tensegrity mechanisms with different number of cells bounded by ribs (n_c). Reprinted from [15].

The position vectors of the end points of the wires in the rest configuration of the tensegrity wing (*i.e.*, at 0° twist) are classified by indices i and j. The index $i \in \{0, \ldots, n_c - 1\}$ represents the rib number starting from the wing root ($i = 0$) and increasing in the spanwise

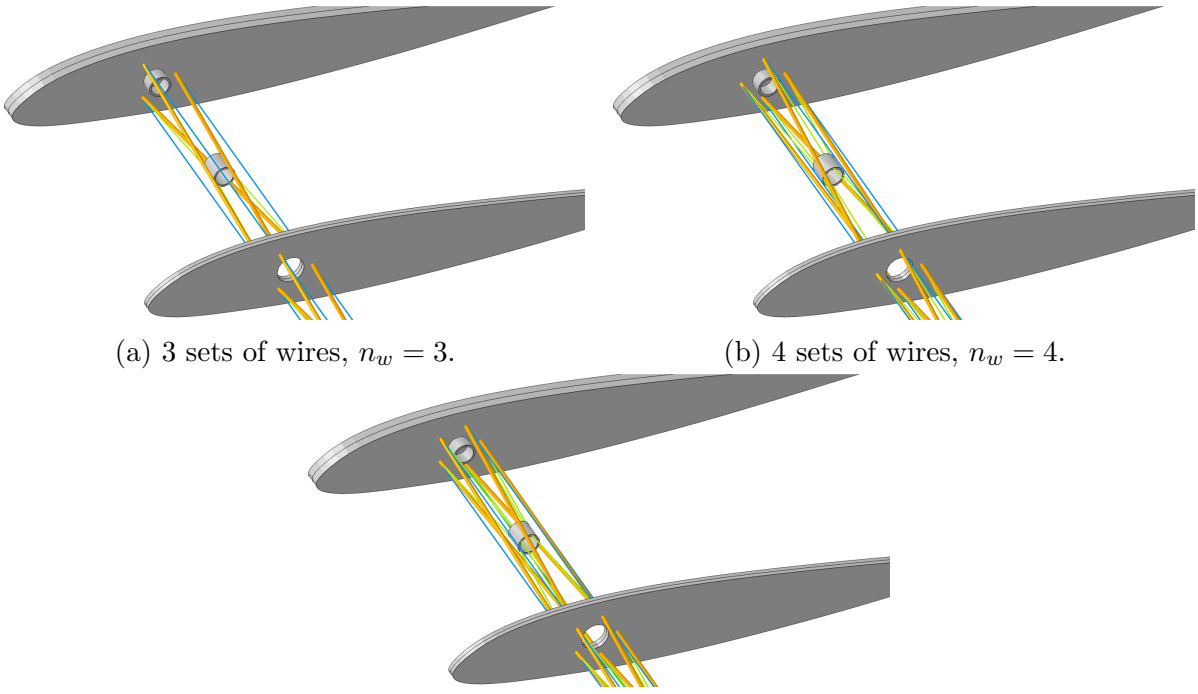

(a) 3 sets of wires, $n_w = 3$.

(b) 4 sets of wires, $n_w = 4$.

(c) 5 sets of wires, $n_w = 5$.

Figure 5.5: Torsional tensegrity mechanisms with different number of wire sets (n_w). The central spar is omitted to enable a better display of the wire members. Reprinted from [15].

direction for each rib until ending at the wing tip ($i = n_c - 1$). The distance between each pair of ribs shown in Fig. 5.3 is given by $s/(2n_c)$. The wingspan s includes the overall wing of an aircraft, but the model has a length of $s/2$ from wing root to tip because only one side is considered in this study. The index $j \in \{0, \ldots, n_w - 1\}$ represents the wire set number starting at the set that radially coincides with the x-axis and increases in the counterclockwise direction of the xy-plane. The wire sets are evenly distributed in a circular patterned centered at the spar; thus, the angle between each wire set is given by $2\pi/n_w$. Other size parameters influencing the wire network arrangement include the axial length of the rings l_r, the radial distance between the wire end points and central axis of the spar R, and the middle radius of the rings r. While l_r is fixed, R and r are both directly proportional to the radius of the spar r_s, a variable explored in the DOE study presented in Section 5.2.

The location of the wire end points are defined using vectors denoted as $\mathbf{p}_{ij}$, $\mathbf{m}_{ij}$, $\mathbf{n}_{ij} \in \mathbb{R}^3$. These vectors are located as indicated in Fig. 5.3. The position vectors components are

defined based on the following formulas [43]:

$$\mathbf{p}_{ij} = \begin{bmatrix} R\cos\left(\frac{2\pi j}{n_w}\right) \\ R\sin\left(\frac{2\pi j}{n_w}\right) \\ \frac{si}{2n_c} \end{bmatrix},$$

$$\mathbf{m}_{ij} = \begin{bmatrix} r\cos\left(\frac{2\pi j}{n_w}\right) \\ r\sin\left(\frac{2\pi j}{n_w}\right) \\ \frac{s}{2n_c}\left(i+\frac{1}{2}\right) - \frac{l_r}{2} \end{bmatrix}, \tag{5.1}$$

$$\mathbf{n}_{ij} = \begin{bmatrix} r\cos\left(\frac{2\pi j}{n_w}\right) \\ r\sin\left(\frac{2\pi j}{n_w}\right) \\ \frac{s}{2n_c}\left(i+\frac{1}{2}\right) + \frac{l_r}{2} \end{bmatrix}.$$

Table 5.1 provides the end points of each wire type while illustrations of the three types are provided in Fig. 5.6. The end points of the longitudinal wires share a common index j, indicating that they hold the same radial coordinate at the rest configuration. This arrangement enables them to extend when the wing undergoes torsional deformation and to restore the wing to its initial configuration after the actuator wires are relaxed. The actuator wires also span the entire tensegrity cell, at rib i, their end points have an index of j while at rib $i+1$, the end points have an index of $j+1$. This arrangement provides the actuator wires with an angular offset from the spanwise direction, which allows them to twist the adjacent cell via contraction. Each stabilizer wire connects a rib to a ring at the middle radius r and the end points of each stabilizer wire share the same index j to ensure stability and hold the entire tensegrity mechanism in a concentric layout with respect to the axial direction of

the spar. Additional stabilizer rings are embedded on the outermost ribs at each end of the wing to maintain the spar aligned to the spanwise direction of the wing. The rings are in contact with the spar but are allowed to rotate about the spar.

Table 5.1: Start and end nodes of the longitudinal, actuator, and stabilizer wires forming the torsional tensegrity mechanism; $i \in \{0, \ldots, n_c - 1\}, j \in \{0, \ldots, n_w - 1\}$.

Wire type	**Start node**	**Finish node**
Longitudinal	$\mathbf{p}_{ij}$	$\mathbf{p}_{i+1\ j}$
Actuator	$\mathbf{p}_{ij}$	$\mathbf{p}_{i+1\ j+1(\mathrm{mod}\, n_w)}$
Stabilizer	$\mathbf{p}_{ij}$ $\mathbf{n}_{ij}$	$\mathbf{m}_{ij}$ $\mathbf{p}_{i+1\ j}$

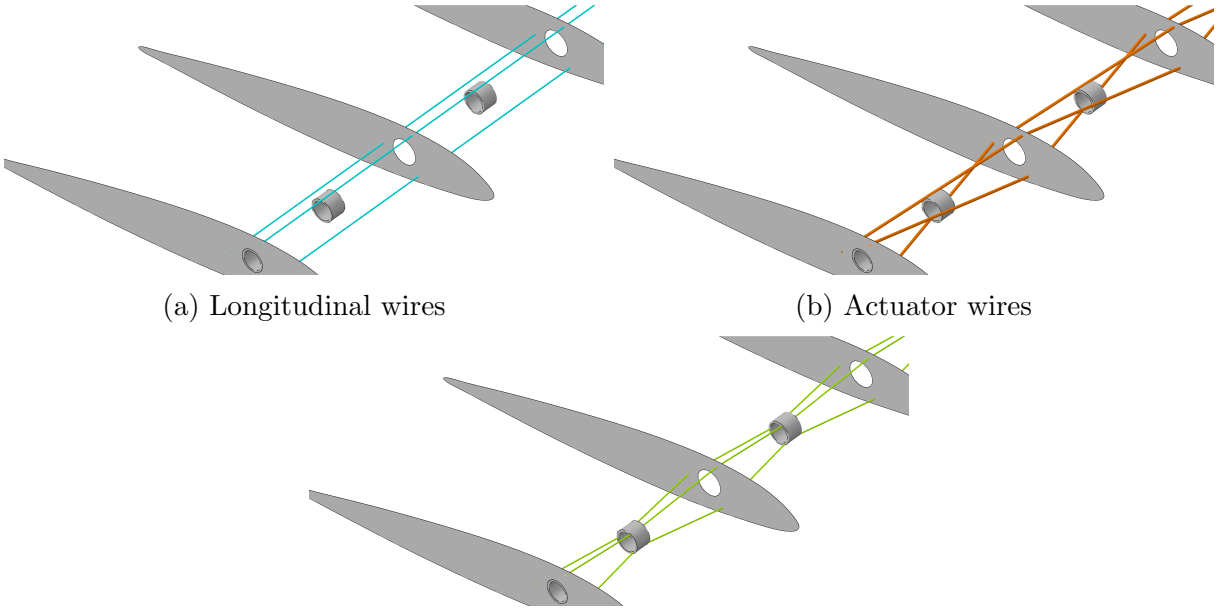

(a) Longitudinal wires

(b) Actuator wires

(c) Stabilizer wires

Figure 5.6: Illustration of the position of the longitudinal, actuator, and stabilizer wires in two cells obtained employing the wire end point connectivity provided in Table 5.1. Reprinted from [15].

Shape memory alloys are strong candidates for the actuator wires in the tensegrity mechanism due to their compact wire configuration and thermally driven material actuation properties. Therefore, these materials are explored for the composition of the actuator wires. In the initial untwisted wing configuration, the SMA wires are in the stretched martensite phase

at the ambient temperature. As the temperature of the SMA wires is increased via Joule heating, reverse transformation initiates at the boundary extended from the the austenite start temperature A_s and then transforms fully to the austenite phase at the boundary extended from the austenite finish temperature A_f. During the reverse transformation into the compact austenite phase, the SMA wires contract lengthwise and simultaneously twist the ribs to provide spanwise torsional motion. During the cooling process, forward transformation starts at the boundary extended from the martensite start temperature M_s, and the transformation of the SMA wires back to being fully in the martensite phase ends at the boundary extended from the martensite finish temperature M_f.

5.2 Shape Memory Alloy Wire Actuation

This study encompasses experimental testing to assess the twisting capability of the proposed wing design. A preliminary prototype of the tensegrity twisting wing was fabricated by undergraduate students from the Mechanical and Aerospace Engineering Department at the University of California, Irvine. The wing prototype includes wooden ribs trimmed to the shape of the Falcon airfoil using laser cutting technique. The central spar utilizes an aluminum rod that extends spanwise through each rib. Composed of aluminum wires, the stabilizer and longitudinal wires are bounded by plastic stabilizer rings. The preliminary wing prototype demonstrates twisting motion through manual modulation of actuator wire tension.

In this work, SMA wires are integrated into the wing prototype to enable twisting capabilities through SMA actuation. The SAES Getters SmartFlex®, 0.3 mm thick, trained SMA wire actuator is used. Joule heating is achieved using an external 6V electric battery as shown with the setup in Fig. 5.7(a). Each battery terminal is connected to the SMA wire at the wing root and the wing tip, respectively, through a pair of electrical wire clamps. Upon

the establishment of the connection to complete a closed circuit, an electrical current is sent through the SMA wire to increase the SMA temperature. The heating induces contraction in the SMA wire length due to the reverse transformation into the martensite phase from its initial austenite phase. Figure 5.7(b) shows the wing twisting motion enabled by SMA wire actuation in the initial, partially twisted, and fully twisted configurations from top to bottom, respectively. Observations from the testing also exhibit quiet, spark-free, and debris-less actuation. After reaching the fully twisted configuration, the electrical connection between the SMA wire and the battery is removed. A combination of natural and forced convection is employed to cool the SMA wire to the ambient temperature. The SMA wire stretches as it undergoes forward transformation to return to the martensite phase during the cooling process. The tensegrity column returns to its initial untwisted configuration after the SMA wire attains its original length at the ambient temperature. The SMA wire actuation cycle is subsequently repeated for multiple iterations, in which the testing demonstrates consistency in the twisting capabilities of the wing design.

A finite element model of the tensegrity wing is created in `Abaqus CAE`^{TM} to assess the stresses and deformations of the wing in response to aerodynamic and internal actuation loads. The parameterization of the wire positions provided in Section 5.1, along with the assumed wing size of the Carl Goldberg Falcon Mark II UAV, are used to create the finite element model. A half-span rectangular wing model is created using dimensions measured directly from a prototype of the UAV. A `Python`^{TM} script is used to parameterize the underlying tensegrity topology and geometry variables of the various finite element components. The `Abaqus S4R` shell elements (linear 4-node shell elements with reduced integration) are used to represent the ribs and skin of the wing in the finite element model because these components have a relatively small cross-sectional thickness when compared against their planform dimensions. Three-dimensional continuum elements `C3D8R` (eight-node brick elements with reduced integration) are used to model the spar and stabilizer rings. `C3D10` elements (10-node tetrahedral elements) are employed to discretize the rings. Since the

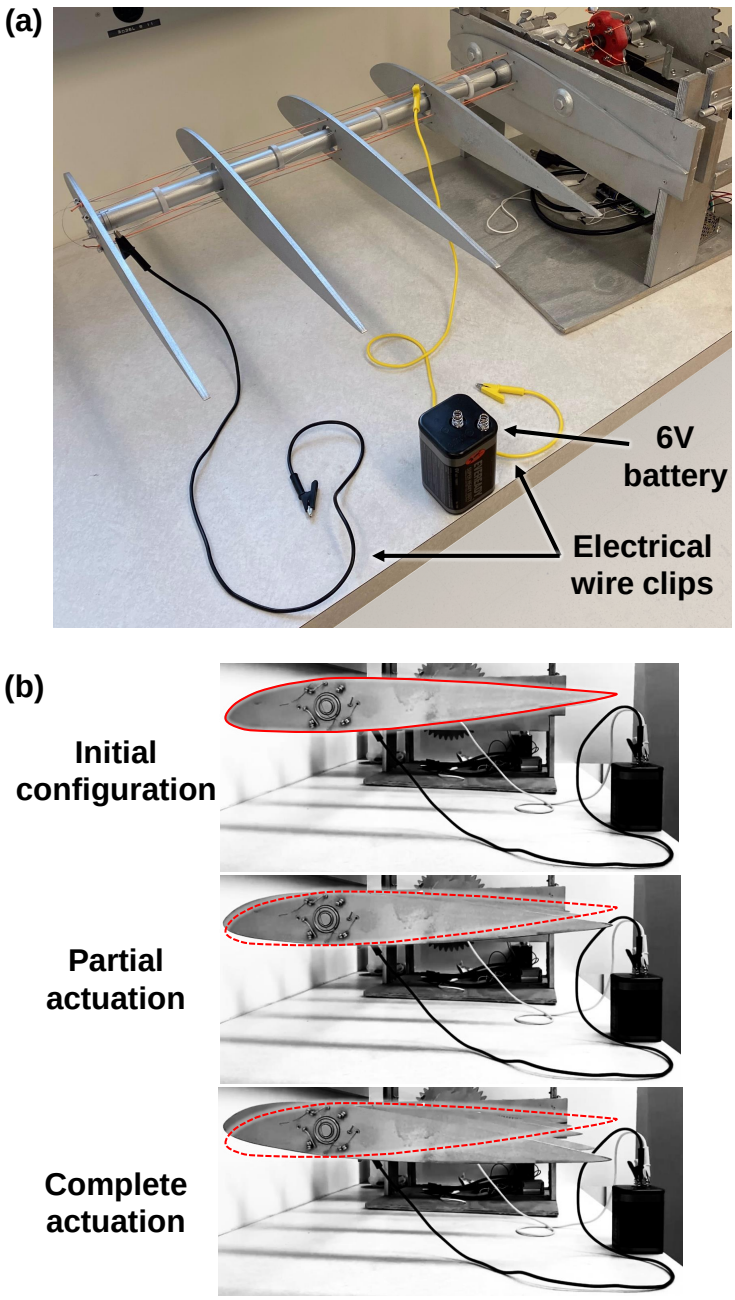

Figure 5.7: Tensegrity wing prototype. (a) Tabletop tensegrity wing prototype. The SMA wires within the tensegrity mechanism are actuated by connecting them to a 6V battery using electrical wire clips. (b) Three configurations of wing prototype during twisting enabled by connecting the SMA actuator wires to the battery. Adapted from [15].

wire members are only subjected to unidirectional tension or compression, and have cross-sectional areas that have much smaller dimensions than their lengths, they are represented

with T3D2 elements (2-node linear 3-D truss). The wires, the ribs, and the rings are laid out such that they are connected at nodal locations. A mesh convergence study is conducted to ensure an appropriate mesh refinement is used before proceeding to the design study presented in the subsequent section. Figure 5.8 provides a sample illustration of the external and internal mesh discretization obtained after the mesh convergence study.

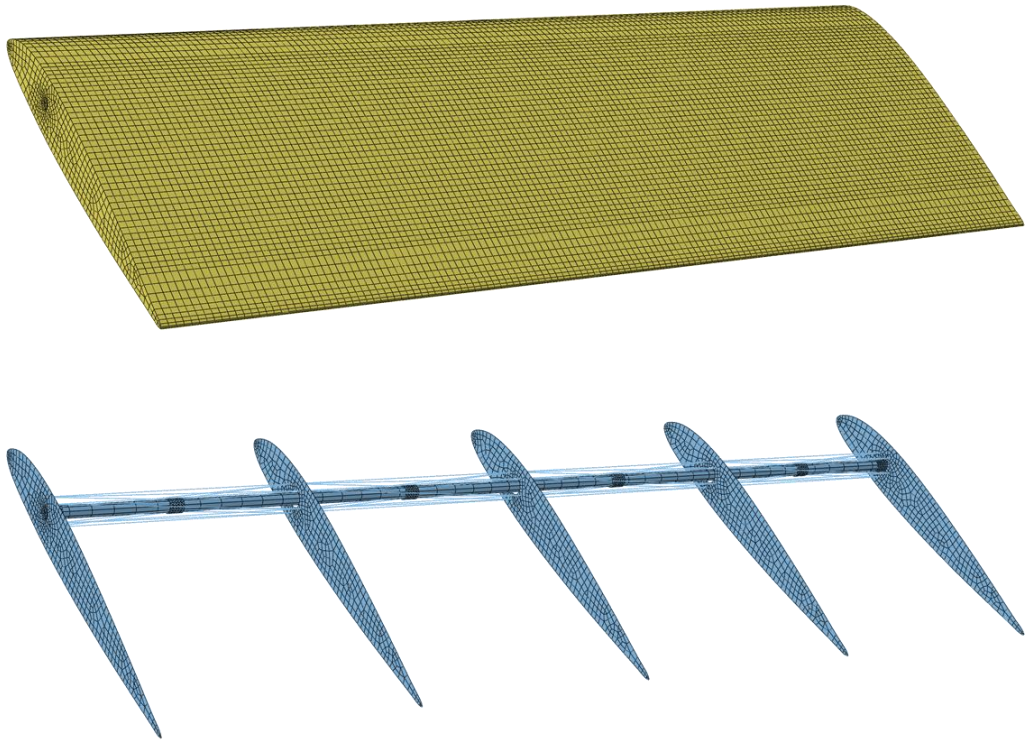

Figure 5.8: Finite element meshes of the wing skin and the internal wing structure obtained from a mesh convergence study. Reprinted from [15].

Figures 5.9(a) and 5.9(b) depict the boundary conditions of the tensegrity wing finite element model. The wing root is fully fixed, representing the wing attachment to the fuselage. Two stabilizing rings are placed at the contact points between the spar and the two outermost ribs. By defining a frictionless and non-penetratble contact interaction between the spar, the inner face of the ring, and the root rib, the spar movement was restricted to only rotations about its axis. Alternatively, a tied constraint was defined between the spar, its corresponding ring, and the tip rib. To allow the rings to rotate freely while remaining concentric to the spar,

another non-penetrable and frictionless contact interaction is defined between the stabilizer rings inner face and the circumferential face of the spar.

Another boundary condition applied in the FEA model addresses the external aerodynamic loads. The pressure coefficient c_p distribution from leading edge to trailing edge on the top and bottom surfaces of the wing at 0° angle of attack ($\alpha = 0°$), shown in Fig. 5.9(a), is obtained from the CFD analysis. The pressure coefficient is defined as:

$$c_p = \frac{p - p_\infty}{\frac{1}{2}\rho v^2}, \tag{5.2}$$

where the quantity $\frac{1}{2}\rho v^2$—the dynamic pressure—is calculated based on standard sea level condition (air density $\rho = 1.225$ kg/m^3) and an air speed of $v = 20$ m/s, which is typical for the reference vehicle, the Carl Goldberg Falcon Mark II UAV. Using Eq. (5.2) and the local value of c_p, the pressure differential values imposed at each node ($\Delta p = p - p_\infty$) is calculated and then mapped onto the external surfaces of the wing as shown in Fig. 5.9(a).

The dynamic-implicit, considering quasi-static deformations analysis step type, allows for reduced computational time while maintaining acceptable accuracy in the final solutions, is chosen in the `Abaqus` simulations. Non-linear geometry (*i.e.*, `NLGEOM` in `Abaqus`) is used to capture larger degree of deformation at different locations on the wing like the skin and wing tip. The user-defined material subroutine (`UMAT`) for SMAs—developed by Karakalas and colleagues [24]—is used to create the shape memory alloy material for the actuator wires. The properties of the $Ni_{51}Ti_{49}$ SMA, listed in Table 5.2, are referenced from works conducted by Karakalas *et al.* [24] and Machairas *et al.* [36]. The phase diagram associated with the material parameters provided in Table 5.2 is shown in Fig. 5.9(c). To facilitate the torsional tensegrity mechanism via actuation of the shape memory actuator wires, a temperature

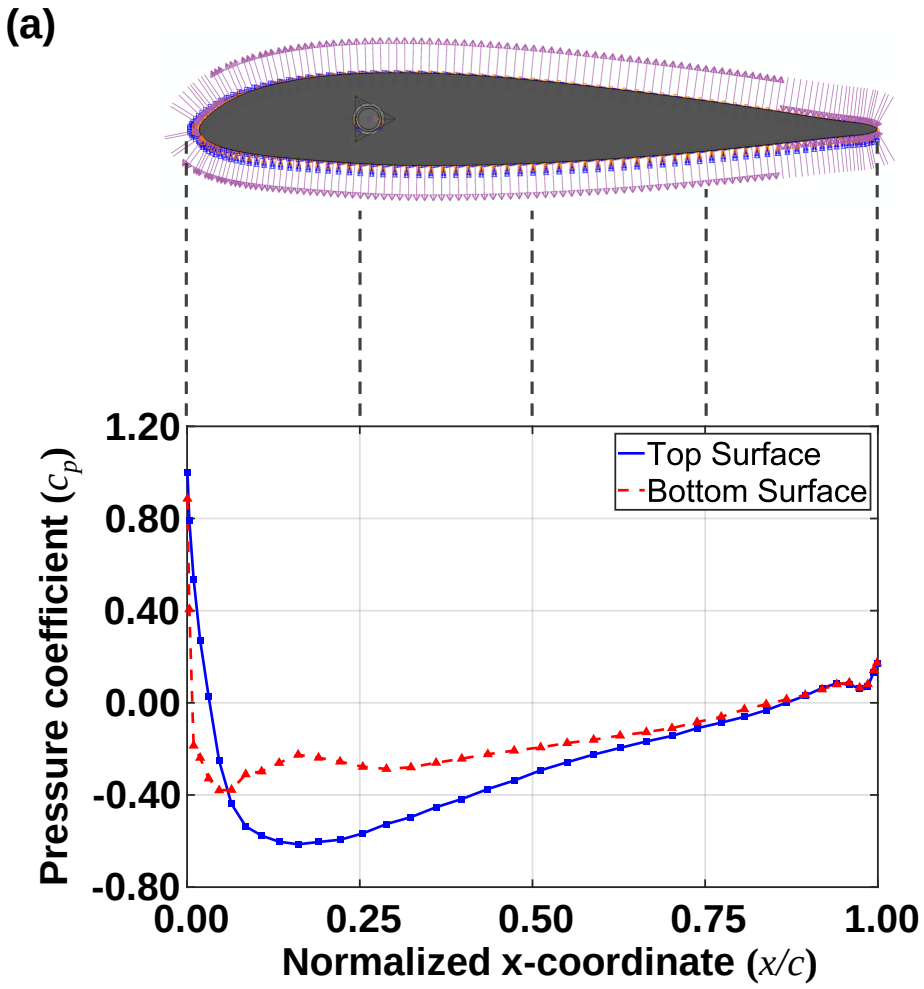
(a)
1.20
0.80
0.40
0.00
-0.40
-0.80
Pressure coefficient (c_p)
0.00
0.25
0.50
0.75
1.00
Normalized x-coordinate (x/c)
Top Surface
Bottom Surface

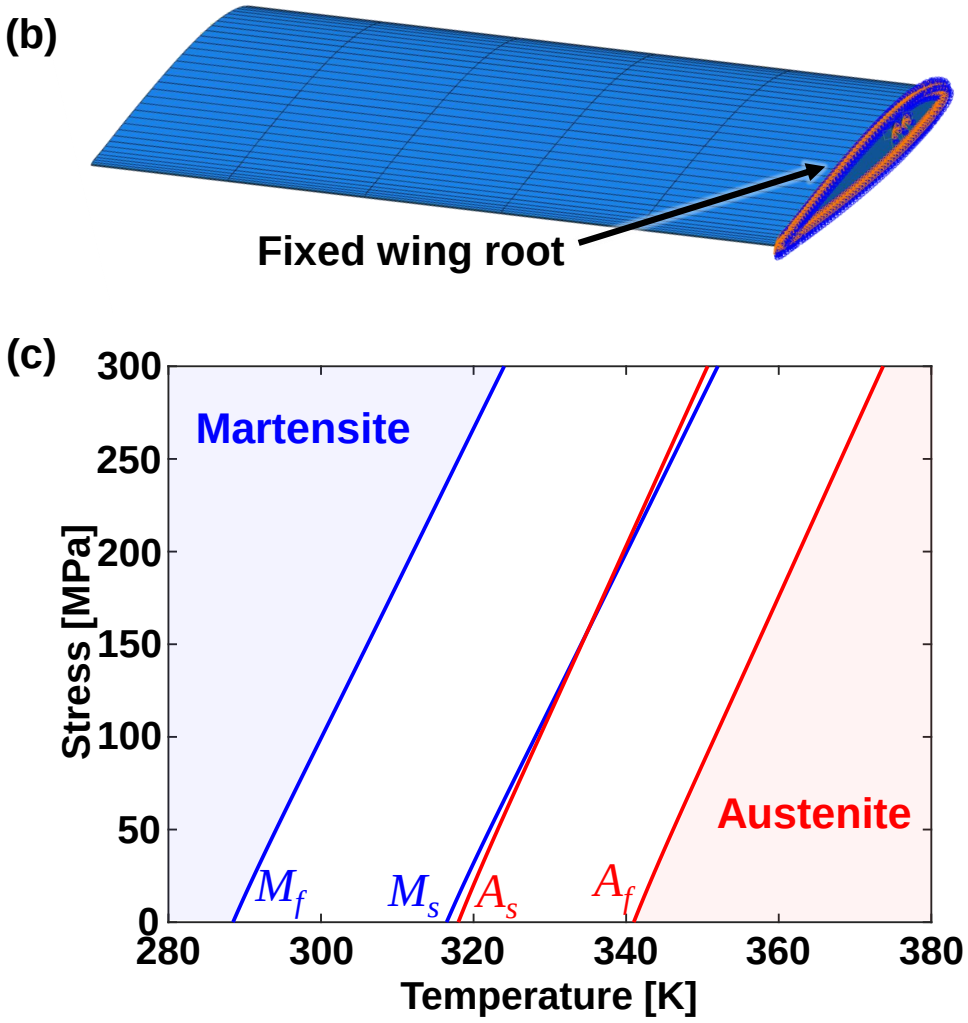

Figure 5.9: Boundary conditions and SMA actuator characteristics. (a) Pressure coefficient distribution for the top and bottom skin surfaces at $\alpha = 0°$ and their mapping into the finite element model using the normalized coordinate along the chord direction x/c. (b) Encastre boundary condition applied at the wing root representing its connection with the fuselage. (c) Phase diagram of the $Ni_{51}Ti_{49}$ SMA based on the material parameters reported in Karakalas *et al.* [24]. Adapted from [15].

increase of 135 K, starting from 238 K, is implemented.

A DOE study is performed to assess the effectiveness of using SMA wires as the actuating mechanism and to determine the critical design drivers. A custom `Python`™ script is used along with `Abaqus CAE`™ to generate the parameterized FEA model and calculate its structural response to aerodynamic loads and SMA actuation. Design parameters include the number of cells n_c and wire sets n_w, the radius of the spar r_s, the thickness of the skin

Table 5.2: Material parameters of a $Ni_{51}Ti_{49}$ SMA obtained from Karakalas *et al.* [24, 36]. The phase diagram associated with these parameters is displayed in Fig. 5.9(c).

Material parameter	**Value**	**Material parameter**	**Value**
Mass density	6500 kg m^{-3}	Strength	880 MPa
Martensite finish transformation temperature M_f	283 K	Martensite start transformation temperature M_s	311 K
Austenite start transformation temperature A_s	313 K	Austensite finish transformation temperature A_f	336 K
Coefficient of thermal expansion of martensite	-2.61×10^{-5} K^{-1}	Coefficient of thermal expansion of austenite	-3.02×10^{-5} K^{-1}
Stress influence coefficient for martensite	8.34 MPa K^{-1}	Stress influence coefficient for austenite	9.02 MPa K^{-1}
Elastic modulus of martensite	25.60 GPa	Elastic modulus of austenite	66.20 GPa
Maximum transformation strain	0.048	Poisson's ratio	0.33
Smooth hardening exponents	0.0924, 0.0736, 0.1118, 0.0756	Back stress	82.05 MPa
Transformation strain exponent	1.29×10^{-8} Pa^{-1}		

t_s, and the thickness of the ribs t_r. Five different levels are considered for each of these five variables, giving a total of 3125 possible design combinations if a full factorial DOE were considered. Since evaluating every possible design combinations is impractical as each simulation takes approximately four hours of computational running time, the Taguchi method is employed to generate a representative design space that can be evaluated to reduce the computation time. A 25×5 Taguchi orthogonal array is created using the algorithm outlined by Leung and Wang [33]. Table 5.3 lists the studied design variables and their respective design values. Additional design variables such as the wire diameters, wing span, and chord length were fixed in this study. The wire diameter values were selected based on the results of previous DOE study [42]. The wing span and chord length are derived from measurements of the reference vehicle, the Carl Goldberg Falcon Mark II UAV shown in Fig. 1.4.

The employed values for the fixed design variables are summarized in Table 5.4.

Table 5.3: Design parameters considered in the Taguchi (orthogonal) DOE and their associated levels.

Design parameter	**Studied levels**				
Number of cells (n_c)	4	5	6	7	8
Number of wire sets (n_w)	3	4	5	6	7
Skin thickness (t_s) [mm]	1.00	1.25	1.50	1.75	2.00
Spar radius (r_s) [mm]	4.00	4.50	5.00	5.50	6.00
Rib thickness (t_r) [mm]	4.00	5.00	6.00	7.00	8.00

Table 5.4: Fixed design parameters and their associated values. The chord length and wing half span correspond to those of the Carl Goldberg Falcon Mark II UAV. The remainder parameters are obtained from a previous design study [42].

Design parameter	**Value**
Chord length	25.3 cm
Wing half span	71.1 cm
Diameter of actuator wires	3.25 mm
Diameter of passive wires (longitudinal and stabilizer wires)	0.81 mm
Axial length of the rings (l_r)	10.0 cm

The wing structure is composed of four major material categories, the first one corresponding to the SMA actuator wires. The ribs, spar, and stabilizer rings, which are assumed to be composed of Al 7075-T73 alloy, form the second group. Although in previous studies Ti-6Al-4V demonstrated superior performance, Al 7075-T73, the runner-up and a commonly used aerospace alloy, is chosen for this study due to its lightweight, manufacturability, and economical benefits [42]. The third material group is comprised of the external skin which requires both flexibility and sturdiness. Engineered polymers are the preferred choice for this component category since they offer both morphing capability and stiffness to sustain aerodynamic loads and debris. Sabic 2004-CX3$^{\text{TM}}$ low-density polyethylene (LDPE) is deemed as a suitable candidate based on previously observed performance [42]. Finally, the passive wires (longitudinal and stabilizer) belong in one category and are designated to be made from

the same material. Since these members are the primary load-bearing agents of the tensegrity structure, they need to be made from a metallic alloy. Gr. 5 Ti alloy is considered in this work based on its favorable performance demonstrated in previous DOE studies [41, 42]. Table 5.5 lists the passive material types (*i.e.,* excluding the SMA components) involved in this design study.

Table 5.5: Material parameters assumed for the ribs, spar, rings, skin, and passive wires.

Component	**Material**	**Elastic modulus**	**Poisson's ratio**	**Strength**	**Mass density**
Ribs, spar, and rings	Al 7075-T73	72.0 GPa	0.33	435.0 MPa	2810.0 kg/m^3
Skin	2004CX3 LDPE	0.240 GPa	0.46	10.0 MPa	921.0 kg/m^3
Passive wires	Gr. 5 Ti	113.8 GPa	0.34	880.0 MPa	4430.0 kg/m^3

The finite element model calculates the maximum von Mises stress of each component category at every loading step (increment in temperature in the SMA wires) and the structural mass m_s. The script then detects the loading step in which any of the components reached their failure strength and provides the twist angle Φ at such an onset of failure. The *twist angle per unit mass* (η) is introduced to assess the effectiveness of each design and is defined as follows:

$$\eta = \frac{\Phi}{m_s}. \tag{5.3}$$

The most favorable design from the DOE, which exhibited the highest value of η corresponding to 7.85°/kg, displayed a maximum twist angle Φ of 15.85° and a mass m_s of 2.02 kg without having any components reach their respective failure values. This design ranked highest in both categories of Φ and η, and thus, is deemed as the most favorable. Fig-

ures 5.10-5.14 are the main effect plots of the five design parameters with the mean values of Φ and m_s included for reference. The level of the most favorable design is also indicated in each plot with a red rhombus.

The main effect plots that consider the topological parameters n_c and n_w, which are the number of cells and wire sets respectively, are displayed in Figs. 5.10 and 5.11. The main effect plots for structural mass clearly indicate a proportional relationship between these two variables and the structural mass. For n_c, the twist angle plot also indicates a directly proportional relationship. An inverted V-shape pattern is observed for the twist angle plot of n_w and the four wire sets design delivered the most favorable outcome.

Figures 5.12-5.14 provide the main effect plots resulting from varying the three variables: skin thickness t_s, spar radius r_s, and rib thickness t_r. The structural mass plots in Figs. 5.13 and 5.14 show a direct proportion between these design parameters and structural mass m_s. A parabolic-like response is observed in Fig. 5.12. The main effect plot associated with the influence of the spar radius shows a directly proportional relation between r_s and Φ, which indicates that a thicker spar will provide a larger twist angle. This result is in agreement with earlier studies [42]. The main effect plot associated with the influence of skin thickness on the twist angle shows an inversely proportional relation between t_s and Φ. A skin thickness of 1.00 mm delivered the highest value of Φ and η. In regards to the rib thickness t_r, the twist angle plot is inconclusive and requires further study as it features an inverted V-shape. The designs with 7.00 mm thick ribs delivered the highest values of twist angle on average. It is reasonable to hypothesize that the number of cells n_c, spar radius r_s, and skin thickness t_s are the dominant design variables since their variations, as shown through the main effect plots, have a much larger impact on the wing performance.

Figures 5.15(a) and 5.15(b) provide displacement contours of the most favorable design at its initial configuration, at 50% deformation, and at 100% deformation. Slight warpage and wrinkles on the skin surface can be observed from these figures. This phenomenon

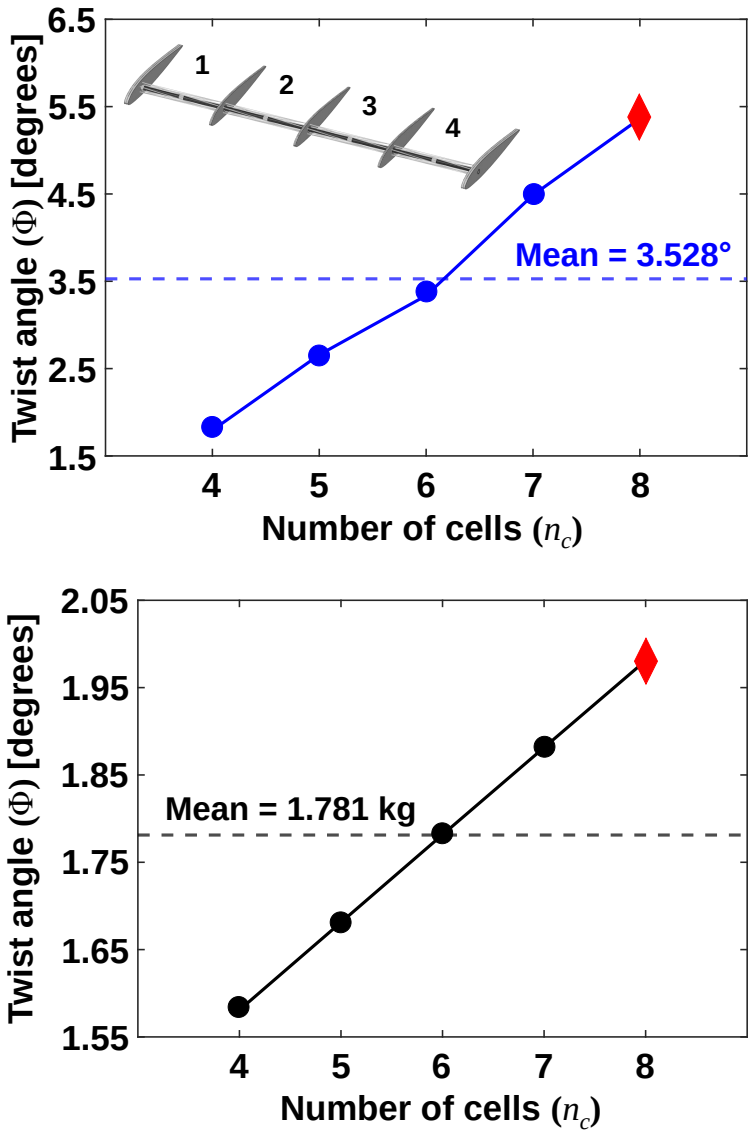

Figure 5.10: Main effect plots of twist angle and mass in terms of number of cells n_c. The red rhombus indicates the level that provides the highest twist angle per unit mass η. Adapted from [15].

can cause the highly undesirable scenario of turbulent flow development and drag increase. Composites or pre-strained polymer sheets are both suitable solutions to this issue and have previously been studied and reported in literature [22, 57]. As the design develops, both of these concepts will be considered future optimization study. The martensite volume fraction variation of one SMA actuator wire of the most favorable design is provided in Fig. 5.15(c) for the entire heating-cooling cycle. This martensite volume fraction vs. temperature plot

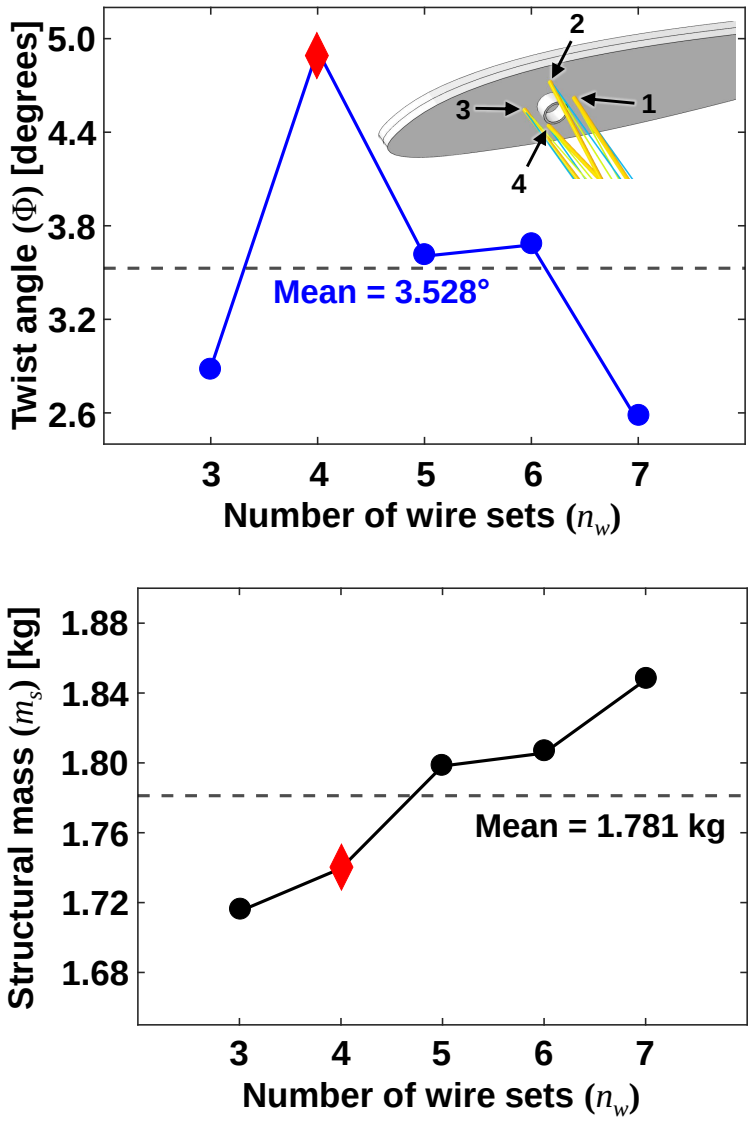

Figure 5.11: Main effect plots of twist angle and mass in terms of number of wires n_w. The red rhombus indicates the level that provides the highest twist angle per unit mass η. Adapted from [15].

shows that only a small change in martensite volume fraction (1 to approximately 0.94) is required to twist the wing by a large amount. Table 5.6 summarizes the design and response parameters of this wing design.

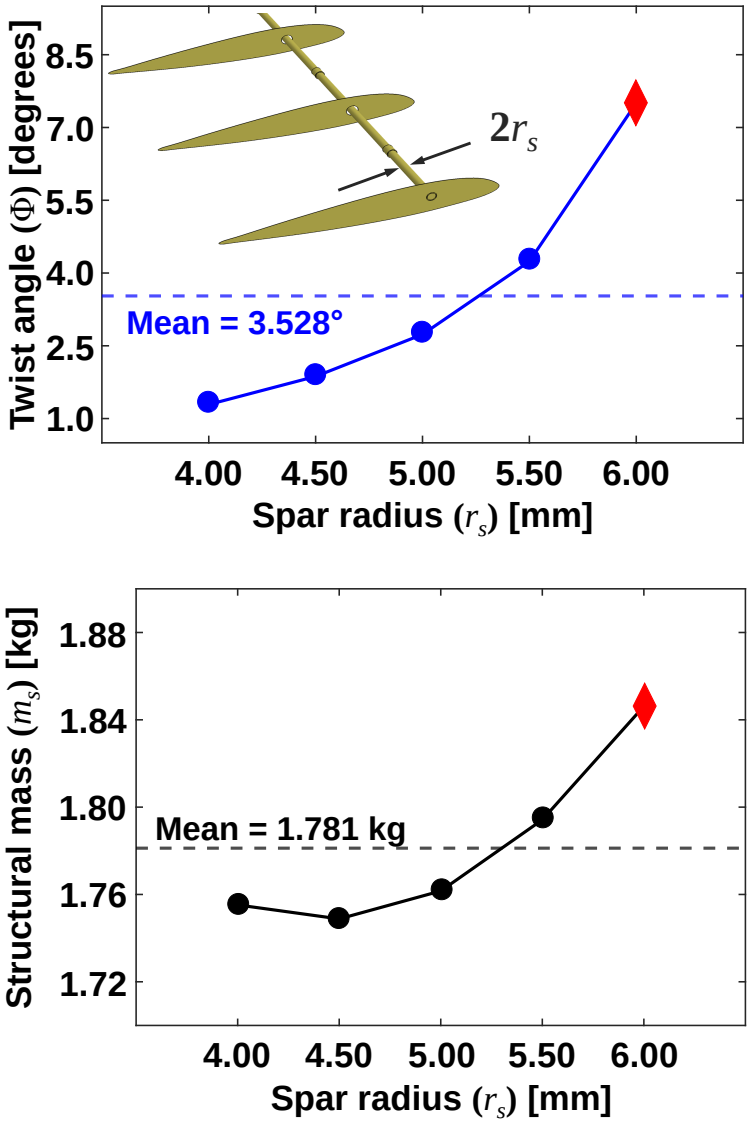

Figure 5.12: Main effect plots of twist angle and mass in terms of spar radius r_s. The red rhombus indicates the level that provides the highest twist angle per unit mass η. Adapted from [15].

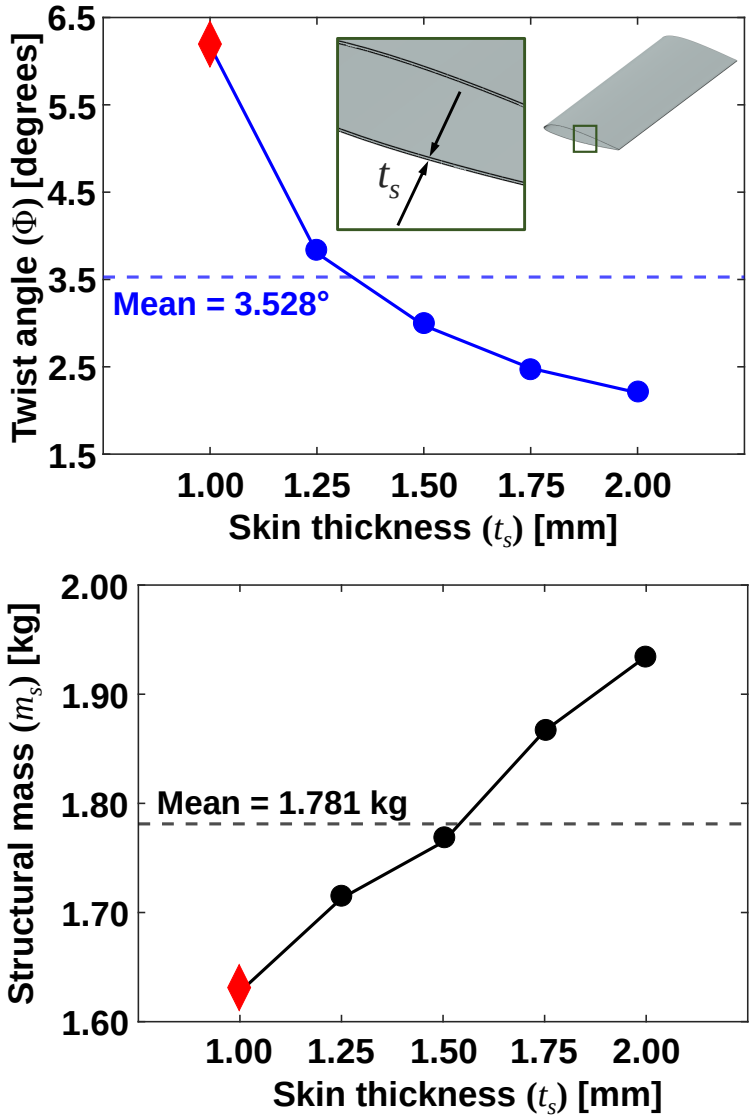

Figure 5.13: Main effect plots of twist angle and mass in terms of skin thickness t_s. The red rhombus indicates the level that provides the highest twist angle per unit mass η. Adapted from [15].

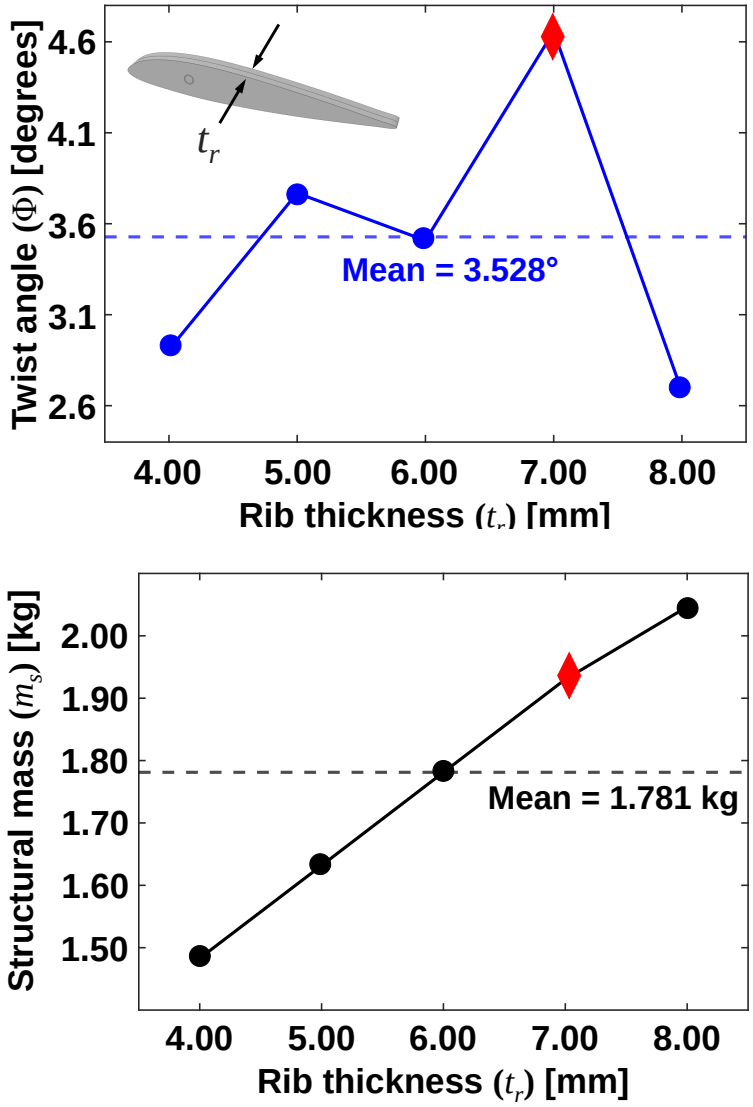

Figure 5.14: Main effect plots of twist angle and mass in terms of rib thickness t_r. The red rhombus indicates the level that provides the highest twist angle per unit mass η. Adapted from [15].

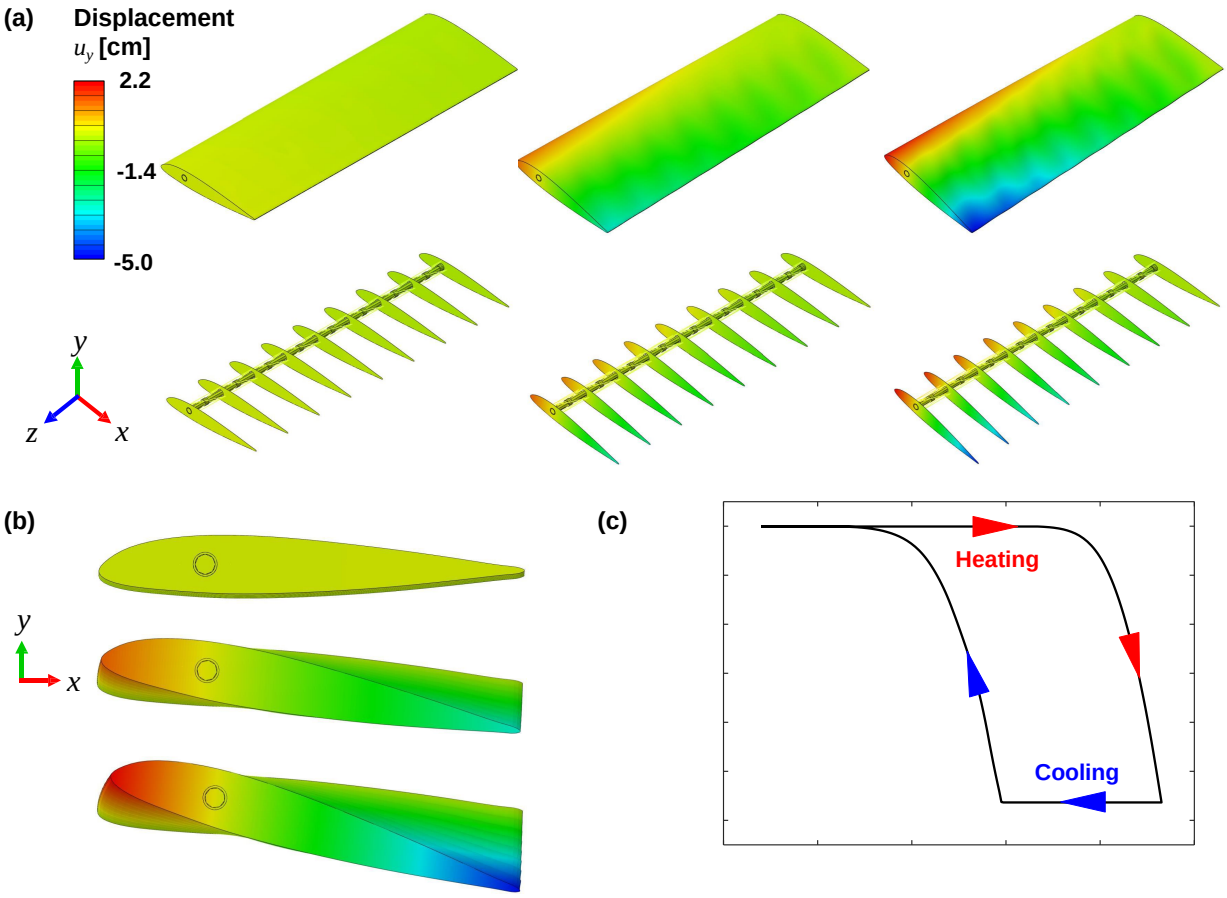

Figure 5.15: Most favorable design analyzed in the DOE. (a) and (b) Displacement contour plots at different configurations during twisting. The most favorable design is selected based on the highest achievable twist angle per unit mass η. (c) Martensite volume fraction variation vs. temperature for an SMA actuator wire during a heating and cooling cycle for the most favorable design. The design and response parameters of this twisting wing are provided in Table 5.6. Reprinted from [15].

Table 5.6: Design and response parameters of the most favorable design studied in the DOE. Deformation contour plots of this design are provided in Fig. 5.15.

Design Parameter	**Value**	**Response Parameter**	**Value**
Number of cells (n_c)	8	Twist angle (Φ)	15.85°
Number of wire sets (n_w)	4	Structural mass (m_s)	2.02 kg
Skin thickness (t_s)	1.00 mm	Twist angle per unit mass (η)	7.85°/kg
Spar radius (r_s)	6.00 mm		
Thickness of ribs (t_r)	7.00 mm		

Chapter 6

Conclusions and Suggested Future Work

6.1 Conclusions

[1] [2] [3] This thesis presented the modeling, design exploration, and optimization of novel shape memory alloy (SMA) axial actuators through the establishment of a computational design framework, employment of a machine learning-assisted approach, and implementation of

[1]Portions of this chapter are reprinted or adapted from [Weilin Guan and Edwin A. Peraza Hernandez, 2020, "Design framework for multi-section shape memory alloy axial actuators considering material and geometric uncertainties," Proceedings of the ASME 2020 International Design Engineering Technical Conferences and Computers and Information in Engineering Conference, DETC2020-22683. https://doi.org/10.1115/DETC2020-22683]. Figures and texts are reprinted by permission of the American Society of Mechanical Engineers.

[2]Portions of this chapter are reprinted or adapted from [Weilin Guan, Hasitha J. Hewakuruppu, and Edwin A. Peraza Hernandez, 2021, "Machine learning-assisted modeling and design optimization of hybrid shape memory alloy axial actuators," Proceedings of the ASME 2021 Conference on Smart Materials, Adaptive Structures and Intelligent Systems, SMASIS2021-68340. https://doi.org/10.1115/SMASIS2021-68340]. Figures and texts are reprinted by permission of the American Society of Mechanical Engineers.

[3]Portions of this chapter are reprinted or adapted from [Weilin Guan, Nguyen K. Pham, and Edwin A. Peraza Hernandez, 2021, "Design exploration of a tensegrity twisting wing enabled by shape memory alloy wire actuation," Proceedings of SPIE Smart Structures/NDE 2021, Active and Passive Smart Structures and Integrated Systems XV, 1158809, virtual conference. https://doi.org/10.1117/12.2582829]. Figures are reprinted by permission of the American Institute of Aeronautics and Astronautics, Inc.

SMA wire actuation to enable a morphing wing. The hybrid SMA actuators are formed by multiple wire sections connected in series, where the length and cross-sectional area of each wire section were design variables. The geometric dimensions and the material distributions were modulated so that the actuation response approximates a target displacement vs. temperature path that is not attainable with monolithic SMA wire with a single section. Constraints on the length-to-diameter aspect ratio and stress of the wire sections and uncertainty in the geometric and material parameters of the actuator were incorporated. A reduced-order numerical model for the hybrid SMA actuators that allowed for efficient design evaluations was derived and implemented in `Matlab`®.

To circumvent potential convergence issues and the computational inefficiency of the structural model for these actuators, a regression model consisting of an ensemble of decision trees was employed as the design evaluator of the thermomechanical response of the hybrid SMA actuators. After model training, a validation test for two-section hybrid SMA actuators performed with 5000 design samples demonstrated R^2 values of 0.99983 for heating and 0.99979 for cooling, which indicates that the surrogate model exhibited high accuracy. The trained surrogate model was used as the design evaluator for the design optimization of hybrid SMA actuators, which enables the reduction in labor, time, and cost. The surrogate-based optimization approach was demonstrated through the synthesis of hybrid SMA actuators capable of exhibiting prescribed displacement vs. temperature target actuation paths.

Subsequently, the work on application of SMA axial actuators extended to the modeling, prototyping, simulation, and design exploration of a twisting wing enabled by an internal tensegrity mechanism equipped with SMA wire actuation. An internal tensegrity column mechanism formed by the ribs and the central spar joined by a wire network was incorporated along the span of the wing to enable control surface-free torsional morphing. Shape memory alloy wires provided a lightweight option for the actuation of the tensegrity mechanism. This wing concept provided modulation of aerodynamic characteristics such as lift and

drag through torsional deformation while maintaining a smooth and continuous outer wing surface. It was demonstrated through CFD analyses that the lift-to-drag ratios are improved for the twisting wing over a comparable conventional wing with a flap. The parameterization and connectivity of the SMA-enabled tensegrity mechanism were introduced for experimental and computational analyses to assess the twisting capabilities of the tensegrity mechanism and the feasibility of SMAs as the means for actuation. Shape memory alloy wires were integrated into the tensegrity mechanism to rotate the ribs co-axially to the central spar through actuation (contraction) induced by Joule heating. The wing torsional deformation triggered by SMA wire actuation was demonstrated through a fabricated tensegrity wing prototype equipped with commercially obtained SMA wire actuators. A finite element model was subsequently devised to analyze the maximum stress experienced by the wing components, structural mass of the twisting wing, and the maximum attainable twist angle. A Taguchi (orthogonal) DOE study was performed to analyze the effects of altering the topological and geometrical design parameters of the wing on the twist angle and structural mass. The most favorable design analyzed in the DOE provided a substantial 15.85° total twist angle without any material failure and had a mass of 2.02 kg. The obtained twist angle was comparable to the twist angle observed from the testing of the tensegrity twisting wing prototype with integrated SMA wire actuators. Accordingly, both experimental and computational analyses demonstrated the twisting capabilities of the SMA-enabled tensegrity wing. The design study results provided an understanding towards the influence of each design parameter to facilitate design optimization in future work.

6.2 Suggested Future Work

The next phase of this research entails the application of the machine learning-assisted model towards hybrid SMA actuators with more than two sections to demonstrate the benefit of

circumventing the iterative structural simulation process for the more complex design of such actuators. Future work includes the prototype fabrication of the hybrid SMA actuators considering tensegrity twisting wing application for experimental validation. The fabrication of the hybrid SMA actuators entails aligning various commercially available SMA wire products concentrically and connecting the adjacent wire sections axially using metallic wire crimp connectors secured to the wire ends. Potential applications of the novel hybrid SMA actuators extend to robotic components, surgical instruments, solar tracking devices, and self-deployable structures that can benefit from using such compact and lightweight actuators while also requiring precise compliance with a desired actuation path. Additionally, the presented twisting wing design implementing hybrid SMA actuators is to be applied to an unmanned aerial vehicle, in which flight and wind tunnel testing are to be conducted to characterize the physical performance of the presented design. Subsequent work entails the characterization and feasibility studies of the actuation speed of the SMA actuators and the investigation of heating and cooling schemes that may enable sufficiently fast thermal actuation cycles. Lastly, the scalability of the tensegrity twisting wing enabled by SMA actuation towards larger scale systems is to be investigated.

Bibliography

[1] K. K. Alaneme and E. A. Okotete. Reconciling viability and cost-effective shape memory alloy options – a review of copper and iron based shape memory metallic systems. *Engineering Science and Technology, an International Journal*, 19(3):1582–1592, 2016.

[2] E. Asua, V. Etxebarria, and A. García-Arribas. Neural network-based micropositioning control of smart shape memory alloy actuators. *Engineering Applications of Artificial Intelligence*, 21(5):796–804, 2008. Constraint Satisfaction Techniques for Planning and Scheduling Problems.

[3] A. N. Bucsek, G. A. Hudish, G. S. Bigelow, R. D. Noebe, and A. P. Stebner. Composition, compatibility, and the functional performances of ternary NiTiX high-temperature shape memory alloys. *Shape Memory and Superelasticity*, 2(1):62–79, Mar 2016.

[4] F. T. Calkins and J. H. Mabe. Flight test of a shape memory alloy actuated adaptive trailing edge flap. In *Smart Materials, Adaptive Structures and Intelligent Systems*, volume 50480, page V001T04A007, 2014.

[5] J. E. Cooper, I. Chekkal, R. C. M. Cheung, C. Wales, N. J. Allen, S. Lawson, A. J. Peace, R. Cook, P. Standen, S. D. Hancock, and G. M. Carossa. Design of a morphing wingtip. *Journal of Aircraft*, 52(5):1394–1403, 2015.

[6] Y. Dong, Z. Boming, and L. Jun. A changeable aerofoil actuated by shape memory alloy springs. *Materials Science and Engineering: A*, 485(1):243–250, 2008.

[7] T. W. Duerig, K. Melton, and D. Stöckel. *Engineering Aspects of Shape Memory Alloys*. Butterworth-heinemann, 2013.

[8] M. H. Elahinia. *Shape Memory Alloy Actuators: Design, Fabrication, and Experimental Evaluation*. John Wiley & Sons, 2016.

[9] A. K. Elwaleed, N. A. Mohamed, M. J. M. Nor, and M. M. Mustafa. A new concept of a linear smart actuator. *Sensors and Actuators A: Physical*, 135(1):244–249, 2007.

[10] A. Emiliavaca, C. J. de Araújo, C. R. Souto, and A. Ries. Characterization of shape memory alloy micro-springs for application in morphing wings. *Smart Materials and Structures*, 28(1):015010, Nov 2018.

[11] R. Goyal, R. E. Skelton, and E. A. Peraza Hernandez. Design of minimal mass load-bearing tensegrity lattices. *Mechanics Research Communications*, 103:103477, 2020.

[12] R. Goyal, R. E. Skelton, and E. A. Peraza Hernandez. Efficient design of lightweight reinforced tensegrities under local and global failure constraints. *Journal of Applied Mechanics*, 87(11):111005, 2020.

[13] W. Guan, H. J. Hewakuruppu, and E. A. Peraza Hernandez. Machine learning-assisted modeling and design optimization of hybrid shape memory alloy axial actuators. In *ASME 2021 Conference on Smart Materials, Adaptive Structures and Intelligent Systems*, Sep 2021. Integrated System Design and Implementation.

[14] W. Guan and E. A. Peraza Hernandez. Design framework for multi-section shape memory alloy axial actuators considering material and geometric uncertainties. In *ASME 2020 International Design Engineering Technical Conferences and Computers and Information in Engineering Conference*, Aug 2020. Volume 10: 44th Mechanisms and Robotics Conference (MR).

[15] W. Guan, N. K. Pham, and E. A. Peraza Hernandez. Design exploration of a tensegrity twisting wing enabled by shape memory alloy wire actuation. In *Active and Passive Smart Structures and Integrated Systems XV*, volume 11588, pages 16 – 32. International Society for Optics and Photonics, SPIE, 2021.

[16] D. J. Hartl and D. C. Lagoudas. Aerospace applications of shape memory alloys. *Proceedings of the Institution of Mechanical Engineers, Part G: Journal of Aerospace Engineering*, 221(4):535–552, 2007.

[17] D. J. Hartl, J. H. Mabe, O. Benafan, A. Coda, B. Conduit, R. Padan, and B. V. Doren. Standardization of shape memory alloy test methods toward certification of aerospace applications. *Smart Materials and Structures*, 24(8):082001, Jul 2015.

[18] J. V. Henrickson, K. Kirkpatrick, and J. Valasek. Rapid characterization of shape memory alloy material parameters using computational intelligence methods. In *ASME Conference on Smart Materials, Adaptive Structures and Intelligent Systems*, Sep 2013. V001T01A001.

[19] J. V. Henrickson, R. E. Skelton, and J. Valasek. Shape control of tensegrity airfoils. In *AIAA Guidance, Navigation, and Control Conference*, page 1864, 2016.

[20] W. Huang. On the selection of shape memory alloys for actuators. *Materials & Design*, 23(1):11–19, 2002.

[21] J. Jayender, R. V. Patel, S. Nikumb, and M. Ostojic. Modeling and control of shape memory alloy actuators. *IEEE Transactions on Control Systems Technology*, 16(2):279–287, 2008.

[22] J. J. Joo, G. W. Reich, and J. T. Westfall. Flexible skin development for morphing aircraft applications via topology optimization. *Journal of Intelligent Material Systems and Structures*, 20(16):1969–1985, 2009.

[23] W.-R. Kang, E. H. Kim, M.-S. Jeong, and I. Lee. Morphing wing mechanism using an SMA wire actuator. *International Journal of Aeronautical and Space Sciences*, 13(1):58–63, 2012.

[24] A. A. Karakalas, T. T. Machairas, A. G. Solomou, and D. A. Saravanos. Modeling of partial transformation cycles of SMAs with a modified hardening function. *Smart Materials and Structures*, 28(3):035014, 2019.

[25] A. Kilicarslan, G. Song, and K. M. Grigoriadis. Modeling and hysteresis compensation in a thin SMA wire using ANFIS methods. *Journal of Intelligent Material Systems and Structures*, 22(1):45–57, 2011.

[26] H.-I. Kim, M.-W. Han, S.-H. Song, and S.-H. Ahn. Soft morphing hand driven by sma tendon wire. *Composites Part B: Engineering*, 105:138–148, 2016.

[27] K. Kirkpatrick and J. Valasek. Reinforcement learning for characterizing hysteresis behavior of shape memory alloys. *Journal of Aerospace Computing, Information, and Communication*, 6(3):227–238, 2009.

[28] K. Kirkpatrick and J. Valasek. Active length control of shape memory alloy wires using reinforcement learning. *Journal of Intelligent Material Systems and Structures*, 22(14):1595–1604, 2011.

[29] J.-S. Koh. Design of shape memory alloy coil spring actuator for improving performance in cyclic actuation. *Materials*, 11:2324, Nov 2018.

[30] D. Lagoudas, D. Hartl, Y. Chemisky, L. Machado, and P. Popov. Constitutive model for the numerical analysis of phase transformation in polycrystalline shape memory alloys. *International Journal of Plasticity*, 32–33:155–183, 2012.

[31] D. Lagoudas, J. Strelec, J. Yen, and M. Khan. Intelligent design optimization of a shape memory alloy actuated reconfigurable wing. volume 3984, pages 338–348, 2000.

[32] P. B. Leal, M. A. Savi, and D. J. Hartl. Aero-structural optimization of shape memory alloy-based wing morphing via a class/shape transformation approach. *Proceedings of the Institution of Mechanical Engineers, Part G: Journal of Aerospace Engineering*, 232(15):2745–2759, 2018.

[33] Y.-W. Leung and Y. Wang. An orthogonal genetic algorithm with quantization for global numerical optimization. *IEEE Transactions on Evolutionary Computation*, 5(1):41–53, 2001.

[34] G. Liang, A. Sadeghifard, A. Krishna, J. Lee, and E. A. Peraza Hernandez. Modeling and analysis of a shape memory alloy-based adaptive regulator for thermal management. In *ASME International Electronic Packaging Technical Conference and Exhibition*, volume 59322, page V001T07A002, 2019.

[35] S. Liu, B. B. Kappes, B. Amin-ahmadi, O. Benafan, X. Zhang, and A. P. Stebner. Physics-informed machine learning for composition – process – property design: Shape memory alloy demonstration. *Applied Materials Today*, 22:100898, 2021.

[36] T. T. Machairas, A. G. Solomou, A. A. Karakalas, and D. A. Saravanos. Effect of shape memory alloy actuator geometric non-linearity and thermomechanical coupling on the response of morphing structures. *Journal of Intelligent Material Systems and Structures*, 30(14):2166–2185, 2019.

[37] Z. Min, V. K. Kien, and L. J. Richard. Aircraft morphing wing concepts with radical geometry change. *The IES Journal Part A: Civil & Structural Engineering*, 3(3):188–195, 2010.

[38] J. Mohd Jani, M. Leary, A. Subic, and M. A. Gibson. A review of shape memory alloy research, applications and opportunities. *Materials & Design (1980-2015)*, 56:1078–1113, 2014.

[39] S. D. Oehler, D. J. Hartl, R. Lopez, R. J. Malak, and D. C. Lagoudas. Design optimization and uncertainty analysis of SMA morphing structures. *Smart Materials and Structures*, 21(9):094016, Aug 2012.

[40] E. A. Peraza Hernandez, D. J. Hartl, A. Kotz, and R. J. Malak Jr. Design and optimization of an SMA-based self-folding structural sheet with sparse insulating layers. In *ASME 2014 Conference on Smart Materials, Adaptive Structures and Intelligent Systems*, page V001T01A015, Sep 2014. SMASIS2014.

[41] N. K. Pham and E. A. Peraza Hernandez. Design exploration of a tensegrity-based twisting wing. In *International Design Engineering Technical Conferences and Computers and Information in Engineering Conference*, pages DETC2020–22656. ASME, 2020.

[42] N. K. Pham and E. A. Peraza Hernandez. Modeling and design exploration of a morphing wing enabled by a twisting tensegrity mechanism. In *AIAA Scitech 2021 Forum*, page 0099, 2021.

[43] N. K. Pham and E. A. Peraza Hernandez. Modeling and design exploration of a tensegrity-based twisting wing. *Journal of Mechanisms and Robotics*, 13(3):031019, 2021.

[44] W. Phillips, N. Alley, and W. Goodrich. Lifting-line analysis of roll control and variable twist. *Journal of Aircraft*, 41(5):1169–1176, 2004.

[45] C. Rathmann, T. Remmetz, and D. Kreimeier. Maintenance of shape memory actuator systems - applications, processes and business models. *Procedia CIRP*, 30:84–89, 2015. 7th Industrial Product-Service Systems Conference - PSS.

[46] H. Rodrigue, S. Cho, M.-W. Han, B. Bhandari, J.-E. Shim, and S.-H. Ahn. Effect of twist morphing wing segment on aerodynamic performance of UAV. *Journal of Mechanical Science and Technology*, 30(1):229–236, 2016.

[47] D. J. S. Ruth and D. G. R. Selvamani. *Design Considerations for Shape Memory Alloy-Based Control Applications*, chapter 2, pages 17–31. John Wiley & Sons, Ltd, 2020.

[48] R. N. Saunders, D. J. Hartl, J. G. Boyd, and D. C. Lagoudas. Modeling and development of a twisting wing using inductively heated shape memory alloy actuators. In *Active and Passive Smart Structures and Integrated Systems 2015*, volume 9431, pages 263 – 270. SPIE, 2015.

[49] B. Selden, K. Cho, and H. H. Asada. Segmented shape memory alloy actuators using hysteresis loop control. *Smart Materials and Structures*, 15(2):642–652, 2006.

[50] R. Shirzadeh, K. R. Charmacani, and M. Tabesh. Design of a shape adaptive airfoil actuated by a Shape Memory Alloy strip for airplane tail. In *Industrial and Commercial Applications of Smart Structures Technologies 2011*, volume 7979, pages 223 – 233. SPIE, 2011.

[51] R. Skelton, F. Fraternali, G. Carpentieri, and A. Micheletti. Minimum mass design of tensegrity bridges with parametric architecture and multiscale complexity. *Mechanics Research Communications*, 58:124–132, 2014.

[52] R. E. Skelton and M. C. de Oliveira. *Tensegrity Systems*. Springer, 2009.

[53] D. D. Smith, R. M. Ajaj, A. T. Isikveren, and M. I. Friswell. Multi-objective optimization for the multiphase design of active polymorphing wings. *Journal of Aircraft*, 49(4):1153–1160, 2012.

[54] M. Stevenson, S. D. Waldman, and Y. Lai. Development of a multi-axial mechanical cell stimulator. *Journal of Intelligent Material Systems and Structures*, 21(2):213–220, 2010.

[55] S. Vasista, L. Tong, and K. Wong. Realization of morphing wings: a multidisciplinary challenge. *Journal of Aircraft*, 49(1):11–28, 2012.

[56] C. Velez, S. Kim, M. Babaei, D. K. Patel, C. Knick, G. Smith, and S. Bergbreiter. Rapid prototyping of microactuators by integrating 3D printed polymeric structures with NiTi thin film. In *2020 IEEE 33rd International Conference on Micro Electro Mechanical Systems (MEMS)*, pages 893–896, 2020.

[57] R. Vos, Z. Gürdal, and M. Abdalla. Mechanism for warp-controlled twist of a morphing wing. *Journal of Aircraft*, 47(2):450–457, 2010.

[58] M. Zakerzadeh, H. Salehi, and H. Sayyaadi. Modeling of a nonlinear Euler-Bernoulli flexible beam actuated by two active shape memory alloy actuators. *Journal of Intelligent Material Systems and Structures*, 22(11):1249–1268, 2011.

[59] Y. Zhang and X. Xu. Transformation temperature predictions through computational intelligence for NiTi-based shape memory alloys. *Shape Memory and Superelasticity*, 6(4):374–386, Dec 2020.

Appendix A

List of Symbols

A_f	Austenite finish transformation temperature
A_i	$i \in \{1, \ldots, n\}$; cross-sectional area of the i^{th} wire section
AR_i	$i \in \{1, \ldots, n\}$; length-to-diameter aspect ratio of the i^{th} wire section
AR^*	Minimum allowable aspect ratio
A_s	Austenite start transformation temperature
c	Chord length
C^A	Stress influence coefficient of austenite
C_D	Drag coefficient
c_l	Sectional lift coefficient
C^M	Stress influence coefficient of martensite
C_L	Lift coefficient
c_p	Pressure coefficient
d_{act}	Diameter of actuator wires
d_{pass}	Diameter of passive wires (longitudinal and stabilizer wires)
e	Actuation path error

E^A	Young's modulus of austenite
E^M	Young's modulus of martensite
e_{T}	Displacement error at a temperature step
e_u	Actuation path displacement error
$e_{\Delta u}$	Target displacement error at the end of cooling
F_i	$i \in \{1, \ldots, n+1\}$; nodal force of the i^{th} node
$H_{\min}$	Minimum magnitude of the transformation strain
H_{sat}	Maximum magnitude of the transformation strain
k	Transformation strain exponential parameter
k_0	Constant force applied to the actuator
L	Total actuator length
l_i	$i \in \{1, \ldots, n\}$; length of the i^{th} wire section
l_r	Axial length of the rings
$\mathbf{m}_{ij}$	$i \in \{0, \ldots, n_c - 1\}, j \in \{0, \ldots, n_w - 1\}$; wire end points located at the root side of the rings
m_s	Structural mass
M_f	Martensite finish transformation temperature
M_s	Martensite start transformation temperature
n	Number of wire sections
n_c	Number of cells
n_i	$i \in \{1, 2, 3, 4\}$; smooth hardening exponents
$\mathbf{n}_{ij}$	$i \in \{0, \ldots, n_c - 1\}, j \in \{0, \ldots, n_w - 1\}$; wire end points located at the tip side of the rings
n_w	Number of wire sets
p	Air pressure
p_∞	Ambient pressure, assumed to be 101325 Pa
$\mathbf{p}_{ij}$	$i \in \{0, \ldots, n_c - 1\}, j \in \{0, \ldots, n_w - 1\}$; wire end points located at the ribs

q	Dynamic pressure, calculated at standard sea level condition
q_s	Number of samples
r	Middle radius of the rings
R	Radial distance between the wire end points and the center of the spar
$\mathbf{R}$	$\in \mathbb{R}^n$; residual vector
r_i	$i \in \{1, \ldots, n\}$; radius of the i^{th} wire section
r_s	Spar radius
s^{th}	Number of temperature steps
s	Wing span
T	Actuator temperature
T_{high}	Highest actuator operating temperature
T_{low}	Lowest actuator operating temperature
T	Actuator temperature
t_r	Rib thickness
t_s	Skin thickness
$\mathbf{u}$	$\in \mathbb{R}^n$; vector of nodal displacements
u_{tar}	Target displacement at the end node
v	Air velocity, assumed to be 20 m/s
u_y	Displacement along the wing thickness direction
x_i	$i \in \{0, \ldots, n\}$; distance between the i^{th} node and the fixed end of the actuator
x/c	x-location of point on the airfoil non-dimensionalized by chord length
y/c	y-location of point on the airfoil non-dimensionalized by chord length
α	Angle of attack
α^{th}	Thermoelastic expansion coefficient
Γ	Ratio of cell length along the span direction between the tip cell and the root cell
δ	Flap deflection angle
Δp	Pressure differential value

ε_i	$i \in \{1, \ldots, n\}$; strain of the i^{th} wire section
η	Twist angle per unit mass
$\lambda_{\Delta u}$	Target displacement error factor
ρ	Air density, assumed to be 1.225 kg/m^3
σ_{crit}	Stress below which transformation is $H_{\min}$
σ_i	$i \in \{1, \ldots, n\}$; axial stress of the i^{th} wire section
σ^*	Maximum allowable axial stress
φ	Twist angle of an individual cell
Φ	Total twist angle
ϕ_j	$j \in \{1, \ldots, n-1\}$; length ratio of the $(j+1)^{\text{th}}$ wire section